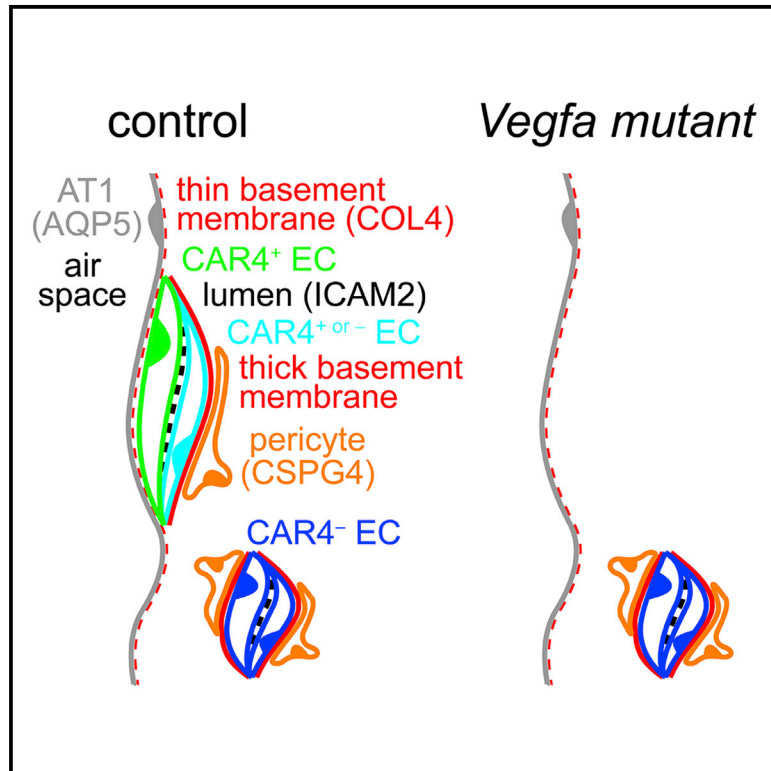# Developmental Cell

Epithelial Vegfa Specifies a Distinct Endothelial Population in the Mouse Lung

Graphical Abstract

Authors

Lisandra Vila Ellis, Margo P. Cain,
Vera Hutchison, ..., Edwin J. Ostrin,
Joshua D. Wythe, Jichao Chen

Correspondence

jchen16@mdanderson.org

In Brief

Using imaging and single-cell RNA-seq, Vila Ellis et al. identify a lung endothelial cell (EC) population with a unique transcriptome, location, morphology, and function in lung development. These ECs are involved in alveolar morphogenesis independent of myofibroblasts.

Highlights

- AT1 epithelial cells express VEGFA, which promotes local alveolar angiogenesis

- scRNA-seq identifies a molecularly distinct lung EC population, labeled by CAR4

- CAR4 ECs display extended morphology and are lost upon epithelial *Vegfa* deletion

- CAR4 ECs contribute to alveolar morphogenesis independent of myofibroblasts

CellPress

Developmental Cell
Article

CellPress

Epithelial Vegfa Specifies a Distinct Endothelial Population in the Mouse Lung

Lisandra Vila Ellis,[1,2] Margo P. Cain,[1,3] Vera Hutchison,[1,4] Per Flodby,[5] Edward D. Crandall,[5] Zea Borok,[5] Bin Zhou,[6] Edwin J. Ostrin,[1,7] Joshua D. Wythe,[8] and Jichao Chen[1,9,*]

[1]Department of Pulmonary Medicine, the University of Texas M. D. Anderson Cancer Center, Houston, TX 77030, USA
[2]Tecnológico de Monterrey – Escuela de Medicina, Monterrey 64710, Mexico
[3]The University of Texas M D Anderson Cancer Center UT Health Graduate School of Biomedical Sciences, Houston, TX 77030, USA
[4]Graduate Program in Developmental Biology, Baylor College of Medicine, Houston, TX 77030, USA
[5]Division of Pulmonary, Critical Care and Sleep Medicine, Department of Medicine and Hastings Center for Pulmonary Research, University of Southern California, Los Angeles, CA 90033, USA
[6]The State Key Laboratory of Cell Biology, CAS Center for Excellence in Molecular Cell Science, Shanghai Institute of Biochemistry and Cell Biology, Shanghai Institutes for Biological Sciences, Chinese Academy of Sciences, University of Chinese Academy of Sciences, Shanghai 200031, China
[7]Department of General Internal Medicine, the University of Texas M. D. Anderson Cancer Center, Houston, TX 77030, USA
[8]Department of Molecular Physiology and Biophysics, Cardiovascular Research Institute, Baylor College of Medicine, Houston, TX 77030, USA
[9]Lead Contact
*Correspondence: jchen16@mdanderson.org
https://doi.org/10.1016/j.devcel.2020.01.009

SUMMARY

The lung microvasculature is essential for gas exchange and commonly considered homogeneous. We show that VEGFA from the epithelium is required for a distinct endothelial cell (EC) population in the mouse lung. *Vegfa* is predominantly expressed by alveolar type 1 (AT1) cells and locally required to specify a subset of ECs. Single-cell RNA sequencing (scRNA-seq) reveals that ~15% of lung ECs are transcriptionally distinct—marked by Carbonic anhydrase 4 (Car4)—and arise from bulk ECs, as suggested by trajectory analysis. Car4 ECs have extensive cellular projections and are separated from AT1 cells by a limited basement membrane without intervening pericytes. Car4 ECs are specifically lost upon epithelial *Vegfa* deletion; without Car4 ECs, the alveolar space is aberrantly enlarged despite the normal appearance of myofibroblasts. Lung Car4 ECs and retina tip ECs have common and distinct features. These findings support a signaling role of AT1 cells and shed light on alveologenesis.

INTRODUCTION

Endothelial cells (ECs) lining the blood vessels fulfill their transport function via region- and organ-specific specialization, such as the artery-capillary-vein relay and the non-leaky blood-brain barrier (Aird, 2007a, 2007b; Potente and Mäkinen, 2017). Additional EC heterogeneity and plasticity are illustrated during development by the opposing duo of leading tip cells and trailing stalk cells within sprouting vessels as well as the

transition of ECs to hematopoietic, mesenchymal, and lymphatic lineages (Dejana et al., 2017; Gariano and Gardner, 2005). These functional and morphological differences in ECs are underlain by distinct gene expression profiles that have been extensively studied in the more tractable vasculature of the post-natal retina and have begun to be systematically tackled across organs using single-cell RNA sequencing (scRNA-seq) (Han et al., 2018; Sabbagh et al., 2018). An emerging theme for cell types that exist in multiple organs, as exemplified by macrophages (Lavin et al., 2014), is that they are endowed with organ-specific molecular signatures.

The pulmonary circulation consists of arterial and venous trees that parallel the branched airways and alveolar ducts and connect distally via a dense network of capillaries covering the gas-exchange alveoli—a high level of spatial coordination that presumably requires precise epithelial-endothelial crosstalk (Morrisey and Hogan, 2010). Although differences between lung macro- and microvasculature as well as lung-specific EC gene expression have been noted (Sabbagh et al., 2018; Stevens et al., 2008), the molecular, cellular, and genetic basis of these differences are poorly understood, especially *in vivo* (Durr et al., 2004). Deciphering lung EC heterogeneity and its developmental origin is also critical to our understanding of bronchopulmonary dysplasia, a severe lung disease often associated with premature birth and characterized by simplified alveoli and dysmorphic vasculature (Thébaud and Abman, 2007).

Our published work shows that (1) the lung capillaries are embedded within grooves of folded alveolar type 1 (AT1) cells, which constitute >95% of the alveolar epithelium; (2) developing AT1 cells, instead of alveolar type 2 (AT2) cells, express a potent angiogenic factor *Vascular endothelial growth factor A* (*Vegfa*); and (3) genetically blocking AT1 cell development decreases alveolar angiogenesis (Yang et al., 2016). These results indicate an instructive role of the alveolar epithelium for lung ECs, although this causality has not been directly tested. In this study, using scRNA-seq and single-cell imaging, conditional and
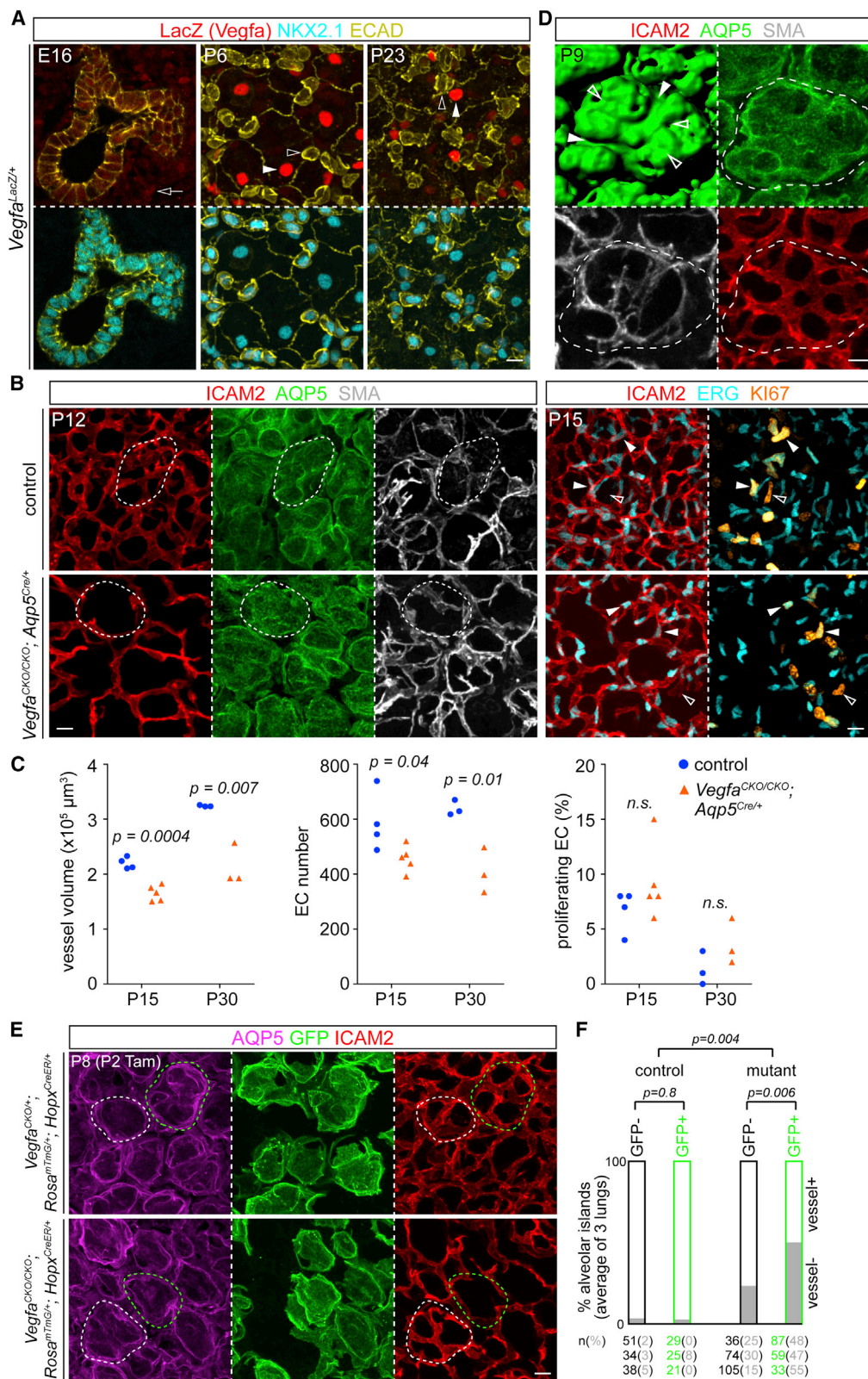
Figure 1. AT1-Derived VEGFA Is Required for Alveolar Angiogenesis Locally

(A) Immunostained lungs with a nuclear LacZ knockin allele of *Vegfa*, representative of at least 2 mice, showing its low mesenchymal expression at E16 (open arrow) and presence in AT1 cells (filled arrowhead) but absence in AT2 cells (open arrowhead). AT1 and AT2 cells are identified by NKX2.1 expression and distinct cell morphology, as outlined by E-cadherin (ECAD). Post-natal lungs are shown as an en face view of the alveolar surface, which better captures AT1 cells.

(legend continued on next page)

mosaic genetic models, and cross-organ comparisons, we found that epithelial-derived VEGFA is required to specify a transcriptionally distinct lung EC population, which features net-like cellular extensions, embraces the epithelial contours, and promotes alveologenesis independent of myofibroblasts—contractile mesenchymal cells generally considered to drive alveologenesis (Boström et al., 1996).

RESULTS

Vegfa Is Predominantly Expressed by AT1 Cells and Locally Promotes Alveolar Angiogenesis

To confirm and extend our previous finding of *Vegfa* expression in developing AT1 cells (Yang et al., 2016), we immunostained developing and mature lungs carrying a nuclear LacZ knockin reporter, *Vegfa^LacZ* (Miquerol et al., 1999). While scattered and at a low level throughout the embryonic lung, the LacZ reporter in post-natal lungs colocalized with nuclei that were positive for NK2 homeobox 1 (NKX2.1)—a lung epithelial lineage factor that we have shown to mark both AT1 and AT2 cells (Little et al., 2019) but were not outlined by cuboidal E-Cadherin (a cell junction protein) staining—a characteristic feature of AT2 cells. This indicated that AT1 cells, instead of AT2 cells, express *Vegfa* in the developing and mature lungs (Figure 1A).

To test the functional relevance of this AT1-specific *Vegfa* expression, we conditionally deleted *Vegfa* in AT1 cells using *Aqp5^Cre* (Flodby et al., 2010; Little et al., 2019), as validated by *in situ* hybridization probing for the deleted exon (Figure S1A). The resulting mutant lungs had sparser microvasculature without apparent changes in alpha-smooth muscle actin (SMA)-expressing myofibroblasts (Figure 1B). This vascular phenotype was quantified as a persistent decrease in vessel volume and EC number (Figures 1B and 1C). However, EC proliferation was not affected (Figures 1B and 1C), suggesting that VEGFA does not function appreciably as a mitogen in the post-natal lung. Interestingly, the remaining vessels in the mutant were not randomly distributed: they failed to occupy the surface of alveolar "islands" that, in a control lung, contained grooves that were associated with myofibroblasts and thus considered secondary septation (Figures 1B and 1D). This raised the possibility that VEGFA is required for a specific subset of alveolar vessels.

The role of AT1-derived *Vegfa* was confirmed using another AT1 cell driver *Hopx^CreER* (Little et al., 2019; Takeda et al., 2011). A single dose of the chemical inducer, tamoxifen, resulted in mosaic recombination in AT1 cells, as indicated by the juxtaposition of recombined GFP+ and unrecombined GFP− AT1 cells using a Cre reporter *Rosa^mTmG* (Muzumdar et al., 2007) (Figure 1E). As expected for the control lung, the alveolar islands (defined in Figure S1B) were invariably covered with vessels with no difference between GFP and non-GFP islands, despite the possible loss of one *Vegfa* allele (Figure 1E). In contrast, up to 50% of the alveolar islands in the *Vegfa* mutant had no vessels—a phenotype more frequently observed for the GFP islands, presumably due to their higher likelihood of recombining both *Vegfa* alleles (Figure 1E). Notably, islands with and without vessel coverage were frequently found to be juxtaposed (Figures 1E and S1B), indicating that AT1-derived VEGFA functions locally to promote vessel formation.

To exclude other functional sources of VEGFA, we conditionally deleted *Vegfa* from AT2 cells and ECs using *Sftpc^CreER* and *Cdh5-CreER*, respectively (Barkauskas et al., 2013; Wang et al., 2010). As expected from the lack of appreciable *Vegfa* expression (Figure 1A), these mutants had normal vasculature (Figures S1C and S1D).

Lastly, we noticed that the AT1-specific *Vegfa* mutant had normal vasculature at post-natal day (P) 2 (Figure S1A), 5 days after the initiation of AT1 cell differentiation at embryonic day (E) 17 (Desai et al., 2014; Li et al., 2018a; Yang et al., 2016). This was likely because Cre recombination occurred after commitment to the AT1 identity—a requirement for a cell-specific Cre driver—such that enough VEGFA protein had accumulated and perdured after DNA deletion. To achieve a more efficient deletion, we resorted to *Shh^Cre*, which targets the entire epithelium during lung specification (Harris et al., 2006). Despite such early targeting, and different from reported results in another epithelial *Vegfa* deletion model (Yamamoto et al., 2007), branching morphogenesis and alveolar morphology up to P3 were unaffected and vascular defects were only observed at E19, concomitant with AT1 cell differentiation (Figures S2A–S2C), suggesting that early embryonic lung angiogenesis is supported by non-epithelial sources of VEGFA or VEGFA-independent mechanisms. The pan-epithelial *Vegfa* mutant recapitulated the AT1-specific *Vegfa* mutant phenotypes, including a decrease

(B) En face view of immunostained lungs, representative of at least 3 littermate pairs, showing impaired alveolar angiogenesis in the AT1-specific *Vegfa* mutant. In the control, vessels (apical membrane marker ICAM2 and nuclear marker ERG) cover alveolar islands (dash; AQP5 together with SMA-expressing myofibroblasts, whereas the remaining vessels in the mutant do not, despite normal coverage by myofibroblasts. Filled arrowhead, KI67-ERG double positive ECs. Non-ECs are also proliferative (open arrowhead).

(C) Quantification showing a lower vessel volume and EC number but comparable proliferation (KI67+) in the mutant (Student's t test; n.s., not significant). Each symbol represents 1 mouse and is the average of 3 regions with hundreds of EC cells counted for each region.

(D) En face view of an immunostained alveolar island (dash) showing the epithelial surface (AQP5 rendering) with grooves containing both myofibroblasts (SMA) and vessels (ICAM2) (filled arrowhead) and those with only vessels (open arrowhead).
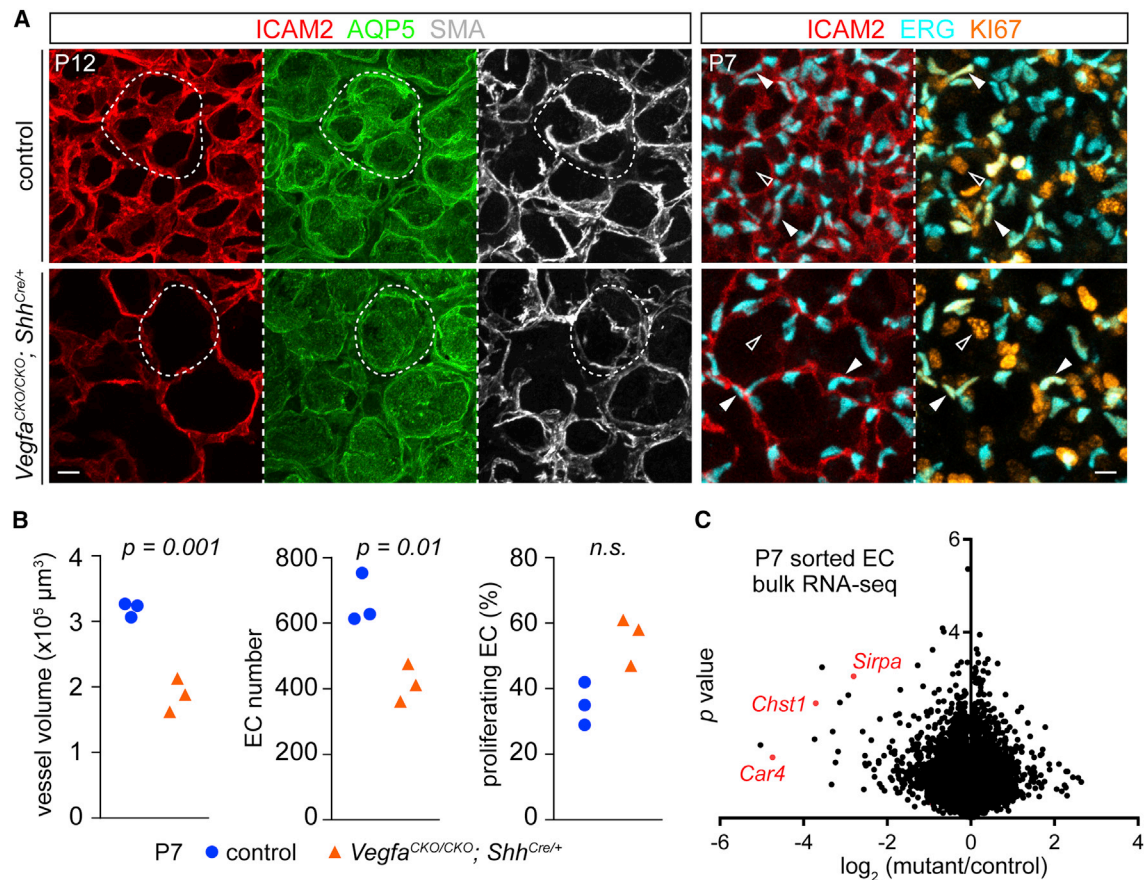
(E) En face view of immunostained lungs, representative of at least 3 littermate pairs, showing that in the mosaic *Vegfa* mutant, juxtaposed recombined alveolar islands (GFP+, green dash) are associated with sparser vasculature than unrecombined ones (GFP−, white dash), whereas both types of alveolar islands have comparable vasculature in the control, as expected. Tam, 200 μg tamoxifen.

(F) Quantification of vessel coverage in 3 littermate pairs. The number (n) of unrecombined (GFP−, black number) and recombined (GFP+, green number) alveolar islands examined in each mouse is tabulated with the percentage of aberrant islands (vessel−) in parenthesis (gray number), whose average is shown as a stack bar graph. Although recombination of the *Rosa* locus does not always match that of the *Vegfa* locus, GFP+ islands are more likely to be aberrant (vessel−) in the mutant (Student's t test), which has more aberrant islands than the control (pooling unrecombined and recombined islands; Student's t test). Control and mutant refer to *Vegfa* heterozygotes and homozygotes in (E).

Scale, 10 μm.

See also Figures S1 and S2.

Figure 2. Epithelial VEGFA Is Required for Alveolar Angiogenesis
(A) En face view of immunostained lungs, representative of at least 3 littermate pairs, showing impaired alveolar angiogenesis in the pan-epithelial *Vegfa* mutant over the alveolar islands (dash, AQP5). Filled arrowhead, KI67/ERG double positive ECs. Non-ECs are also proliferative (open arrowhead). Scale bars, 10 μm.
(B) Quantification showing a lower vessel volume and EC number but comparable proliferation (KI67$^+$) in the mutant (Student's t test; n.s., not significant). Each symbol represents one mouse and is the average of three regions with hundreds of EC cells counted for each region.
(C) Volcano plot of bulk RNA-seq results from sorted lung ECs from 3 littermate pairs. See Table S1 for the complete dataset.
See also Figure S2; Table S1.

in vessel volume and EC number without affecting proliferation as well as the failure to cover alveolar islands where secondary septation normally occurred (Figures 2A and 2B). Interestingly, western blots of P0 whole lungs showed a disproportional loss of the major VEGFA receptor (KDR or VEGFR2) along with its active, phosphorylated form, relative to a nuclear EC marker ERG (ETS transcription factor) (Figure S2D). This could be due to defective VEGFA signaling and/or preferential loss of ECs with a higher level of KDR. Taking into account all the cell-type-specific *Vegfa* mutant models, we concluded that AT1-derived *Vegfa* is required locally for alveolar angiogenesis and possibly regulates a specific EC population in the developing lung. Because of its more robust phenotypes, the pan-epithelial *Vegfa* mutant was used in subsequent analyses.

scRNA-Seq Identifies a Molecularly Distinct Lung EC Population

To understand the molecular basis of the pan-epithelial *Vegfa* mutant phenotype, we used lungs with genetically labeled fluorescent ECs to optimize a cell dissociation and sorting protocol

and found that including CD45 (an immune cell marker) negative selection allowed better separation of ICAM2 (or CD31; both EC markers) positive and negative cells and that ICAM2 selection was consistent with, but more robust than, the more commonly used CD31 selection (Figures S3A and S3B). Bulk RNA-seq comparison of purified ECs from control and pan-epithelial *Vegfa* mutant lungs revealed downregulation of genes that were, intriguingly, recently identified as markers of sprouting tip ECs, such as *Sirpa* and *Chst1* (Figures 2C, S2E, and S2F; Table S1) (Sabbagh et al., 2018). This, together with the established role of *Vegfa* in inducing retinal tip ECs (Gariano and Gardner, 2005) and the non-random distribution of remaining ECs in our AT1-specific and pan-epithelial *Vegfa* mutant lungs, led us to hypothesize that *Vegfa* specifies a subset of ECs in the lung that are analogous to tip ECs in the retina.

To examine this potential lung EC heterogeneity, we performed scRNA-seq on 4,278 sorted P14 lung ECs. Intriguingly, 14% of the sequenced ECs comprised a transcriptionally distinct cluster, which we named Car4 EC because *Carbonic anhydrase 4* (*Car4*) was its most specific marker (Figure 3). All remaining
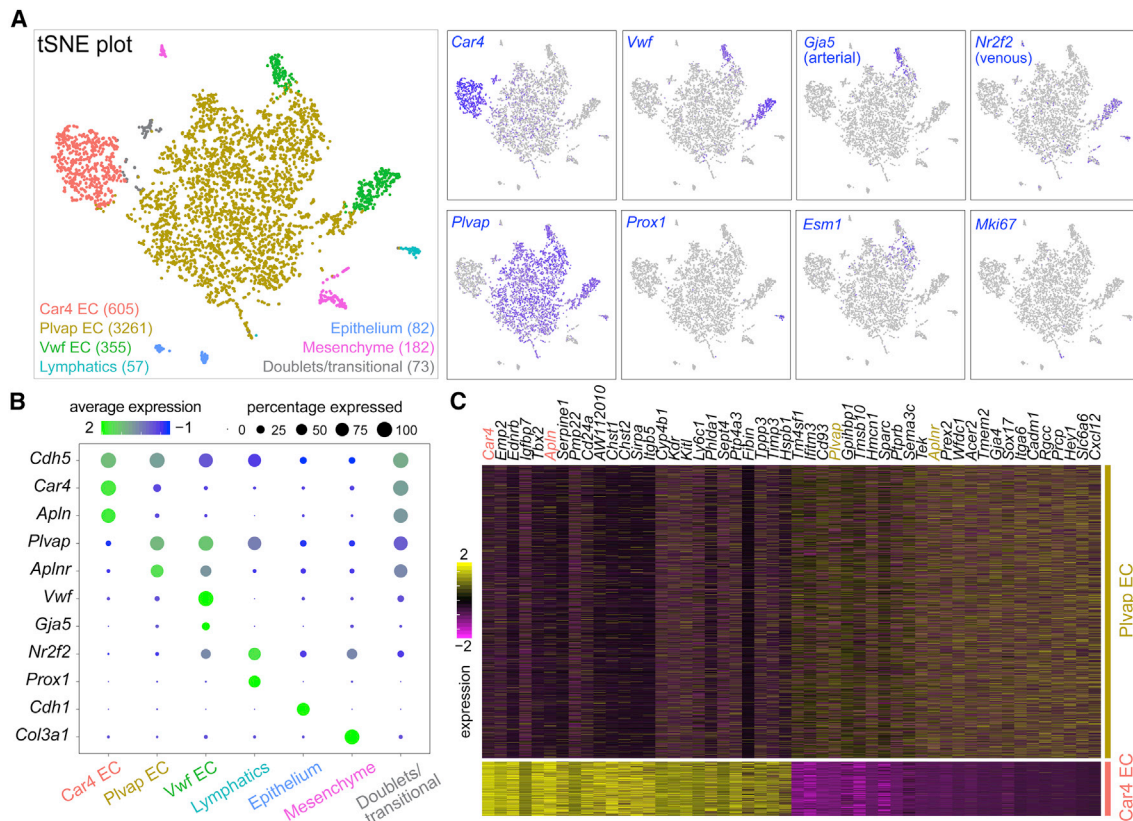
Figure 3. scRNA-Seq Identifies a Distinct Lung EC Population

(A) Left: tSNE plot of scRNA-seq of sorted P14 lung ECs with each cell population color coded and the corresponding cell number shown in parenthesis. Right: population marker expression. Vwf ECs were further divided into arterial cells, marked by *Gja5*, and venous cells, marked by *Nr2f2*. *Esm1* marks a group of Plvap ECs adjacent to the arterial cells, and *Mki67*, a marker of proliferation, is expressed by Plvap ECs but not Car4 ECs.

(B) Dot plot showing population markers. Epithelial and mesenchymal populations are minor contaminants from sorting. A population of doublets or transitional ECs express both *Plvap* and *Car4*.

(C) Heatmap showing top 25 genes comparing Car4 and Plvap ECs. See Table S2 for markers for Vwf and lymphatic ECs.

See also Figures S3–S6; Table S2.

ECs (86%) expressed *Plasmalemma vesicle associated protein* (*Plvap*) and included macrovascular ECs that expressed *Von Willebrand factor* (*Vwf*) (thus named Vwf EC; 8.5% of all ECs) and lymphatic ECs that expressed *Prospero homeobox 1* (*Prox1*) (1.5% of all ECs) (Figures 3A and 3B). Vwf ECs formed 2 subclusters corresponding to arterial or venous macrovascular ECs, as marked by *Gja5* or *Nr2f2*, respectively (Figure 3A). The identity of Vwf and lymphatic ECs were further supported by immunostaining that showed their distinct localization from capillary ECs (Figures S4A and S4B). The bulk (90%) of the *Plvap*-expressing ECs (76% of all ECs) were named Plvap EC for both simplicity and the availability of a PLVAP antibody for tissue localization and had a distinct gene signature from Car4 ECs (Figure 3C; Table S2). We note that *Car4*, *Plvap*, *Vwf*, and *Prox1* were used as population-specific markers but not investigated for their functions in this study.

To investigate the ontogeny of Car4 ECs, we performed scRNA-seq on 851 E17 and 1,570 E19 lung ECs (Figure 4A). Car4 ECs were first detected at E19, coinciding with AT1 cell differentiation (Yang et al., 2016), and did not express the proliferation marker *Mki67*. *Plvap*-expressing ECs constituted all ECs at

E17 and included *Mki67*-expressing proliferative ECs as well as Vwf and lymphatic ECs. The observation that proliferative Plvap ECs predate non-proliferative Car4 ECs supported the possibility that Car4 ECs originated from Plvap ECs. Monocle trajectory analysis (Qiu et al., 2017) showed that Plvap ECs at E17 matured over time and a subset of them became Car4 ECs along a distinct trajectory (Figure 4B). Trajectory heatmaps identified dynamic gene expression patterns, such as high expression of a ribosomal gene *Rpl18a* in immature Plvap ECs—consistent with their rapid growth in embryonic lungs. One gene group showed upregulation before Car4 ECs fully matured and, interestingly, included *Kdr* (or *Vegfr2*), the major receptor for VEGFA, which might confer a higher sensitivity to Vegfa signaling to specify Car4 ECs (Figure 4C; Table S3).

We further investigated the localization of Car4 and Plvap ECs by immunostaining in conjunction with a pan-EC nuclear marker ERG (Fish et al., 2017; Shah et al., 2016). Although predominantly on the cell membrane, both CAR4 and PLVAP also accumulated around the nucleus, allowing assignment of individual ERG nuclei to the Car4 or Plvap ECs (Figure 5A). Intriguingly, Car4 ECs covered the aforementioned alveolar islands that were
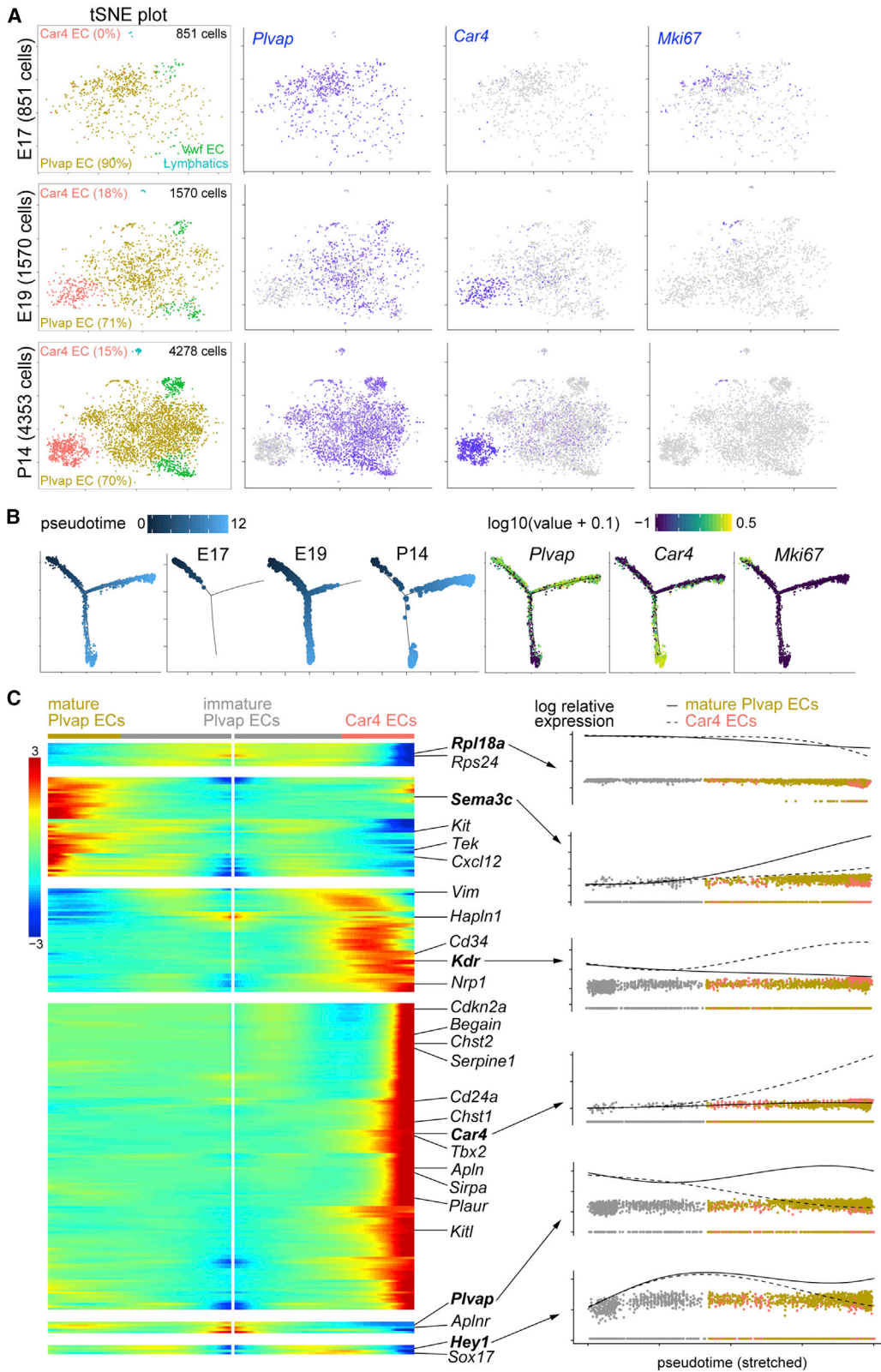
Figure 4. Trajectory Analysis Supports that Car4 ECs Originate from Plvap ECs at E19

(A) tSNE plots of scRNA-seq from purified lung ECs over time, with the populations identified as in Figure 3 and their percentages shown in parenthesis. Car4 ECs were first detected at E19. Plvap ECs, but not Car4 ECs, are proliferative (*Mki67*).

(legend continued on next page)

undergoing secondary septation, whereas Plvap ECs surrounded those islands, a distribution reminiscent of the remaining vessels in both the AT1-specific and pan-epithelial *Vegfa* mutants (comparing Figure 5A with Figures 1B and 2A). This spatial difference in CAR4 and PLVAP staining was also evident for the corresponding nuclei (Figure 5A). Furthermore, although CAR4 staining was abundant, the number of Car4 ECs was under-represented (Figures 3A, 4A, and 5A), a discrepancy between cell number and vessel contribution suggesting that Car4 ECs are disproportionally larger.

Single-Cell Imaging Revealed Extended Car4 EC Morphology

The unique transcriptional profile and tissue distribution of Car4 ECs prompted us to examine their cellular morphology. Unlike the retina vasculature, which can be visualized in two dimension (2D) after flat-mounting the tissue, lung ECs reside in thin tubes winding through a three-dimensional alveolar structure, making it challenging to examine their morphology. To overcome this, we resorted to the sparse cell labeling method that we have used to study the similarly complex AT1 cells (Yang et al., 2016). Specifically, we used a pan-endothelial inducible driver *Cdh5-CreER* (Wang et al., 2010), combined with an optimized, limited dose of tamoxifen, to sparsely label ECs so that individual ECs could be readily demarcated (Figure 5B). As lungs were harvested within 24 h after induction, labeled cells were not intended to be clonally related. We also used a strong reporter $Rosa^{tdT}$ (Madisen et al., 2010) to fill the entire cell body to (1) visualize the nucleus to confirm the intended single-cell labeling and (2) colocalize with the membrane marker CAR4 to identify EC populations. Labeled cells were identified as Car4 ECs if they satisfied two criteria: (1) nuclear tdT (tdTomato) completely overlapped with perinuclear CAR4 staining and (2) cytoplasmic tdT completely aligned with membrane CAR4 staining. In remarkable contrast to Plvap ECs, Car4 ECs were highly branched, often contributing to 5–10 vessel segments, and also much larger, as quantified by measuring the cell perimeter (Figures 5B and 5C). Both Car4 and Plvap ECs had distinct morphology from the non-capillary Vwf ECs, which were elongated along the direction of blood flow (Figure S5A).

Closer examination of $Rosa^{tdT}$-labeled ECs in relation to neighboring Car4 ECs, an apical lumen marker intercellular adhesion molecule 2 (ICAM2), and an adherens junction protein Cadherin 5 (CDH5) showed that (1) the sprawling labeled CAR4⁺ ECs did not exclude other ERG nuclei within the same vessel segments; (2) the labeled CAR4⁻ ECs could be juxtaposed and share a common lumen with CAR4⁺ ECs, the latter being closer to the air space; and (3) although the boundary of labeled cells coincided with CDH5, additional cell junctions were present within the labeled vessel segments (Figures 5B and S5A). These observations suggested that individual lung capillaries are multi-cellular and can be comprised of both CAR4⁺ and CAR4⁻ ECs.

To delineate the spatial relationship between Car4 ECs and non-EC structures, we inspected optical sections of the "slope" of the aforementioned alveolar islands that were captured by whole-mount immunostaining (Figure 5D). Compared to non-Car4 ECs, Car4 ECs were the closest to the air space, as marked by the AT1 membrane marker AQP5, and separated by a thin basement membrane, as marked by Collagen IV (COL4), with no intervening pericytes, as marked by CSPG4 (also known as NG2). The side of Car4-EC-containing vessels that was away from the air space, as well as non-Car4-EC vessels, had a thicker basement membrane and was covered by pericytes.

## Comparison of Retina and Lung ECs Revealed Common and Organ-Specific EC Heterogeneity

The aforementioned similarity of Car4 ECs to tip ECs prompted us to examine tip EC-enriched genes in the distinct subsets of lung ECs. Intriguingly, Car4 ECs specifically expressed *Apln* as well as additional tip EC genes recently identified by scRNA-seq analysis of developing brain ECs, such as *Plaur*, *Serpine1*, *Sirpa*, *Piezo2*, and *Chst1* (Sabbagh et al., 2018) (Figure S4C). Plvap ECs specifically expressed several stalk cell genes including *Aplnr* and *Tek* (also known as *Tie2*) (Figure S4C). However, the analogy of Car4/tip ECs and Plvap/stalk ECs did not extend to other known tip and stalk EC markers, as exemplified by *Esm1* and *Dll4* for tip ECs and *Hes1* and *Flt1* for stalk ECs (Blanco and Gerhardt, 2013) (Figure S4C).

We further compared retina and lung ECs by immunostaining for ESM1, CAR4, and DLL4. As reported (Rocha et al., 2014), ESM1 was restricted to tip ECs in the peripheral retina and excluded from mature vessels in the more central region (Figure S5B). Interestingly, ESM1 was expressed in sporadic ECs near the lobe edge in embryonic lungs, raising the possibility that the lobe edge represents a growing front similar to the peripheral retina. However, this edge-specific expression was lost post-natally and ESM1 was enriched in ECs in a transition zone between capillaries and non-capillaries (Figures S4C and S5B). This area might correspond to a pre-arteriole region because *Esm1*-expressing cells were adjacent to arterial Vwf ECs in the scRNA-seq tSNE (t-distributed stochastic neighbor embedding) plot (Figure 3A). In contrast, CAR4 was not detected in either the tip or stalk ECs in the retina, whereas its expression in the lung initiated at E19, consistent with our time course scRNA-seq analysis (Figures 4 and S5B). Lastly, although *Dll4* regulates tip ECs (Blanco and Gerhardt, 2013), its protein was only slightly enriched in tip ECs and, in the central region, more evident in arteries than veins. Similarly, DLL4 was widely expressed in embryonic lungs but became more concentrated in a cord-like pattern post-natally, possibly corresponding to ECs coalescing into the macrovasculature (Figure S5B).

Next, we examined the morphology of retina ECs in comparison to that of lung ECs using our sparse cell labeling method

(B) Monocle trajectory analysis of Plvap and Car4 ECs. All E17 ECs occupy the initial branch and express *Plvap*, thus called immature Plvap ECs. At E19, ECs begin to split into two distinct branches: one marked by *Plvap* (mature Plvap ECs) and the other one by *Car4* (Car4 ECs); P14 ECs further diverge along these 2 branches. *Mki67* is largely limited to the initial branch.

(C) Trajectory heatmap showing dynamic gene expression patterns. The 3 branches are color coded and form 2 trajectories, both originating from the center. Genes for each pattern are shown; representative genes are highlighted (bold) and their expression values plotted along both trajectories: dash lines for immature Plvap ECs to Car4 ECs and solid lines for immature Plvap ECs to mature Plvap ECs. See Table S3 for the complete gene list for each pattern.
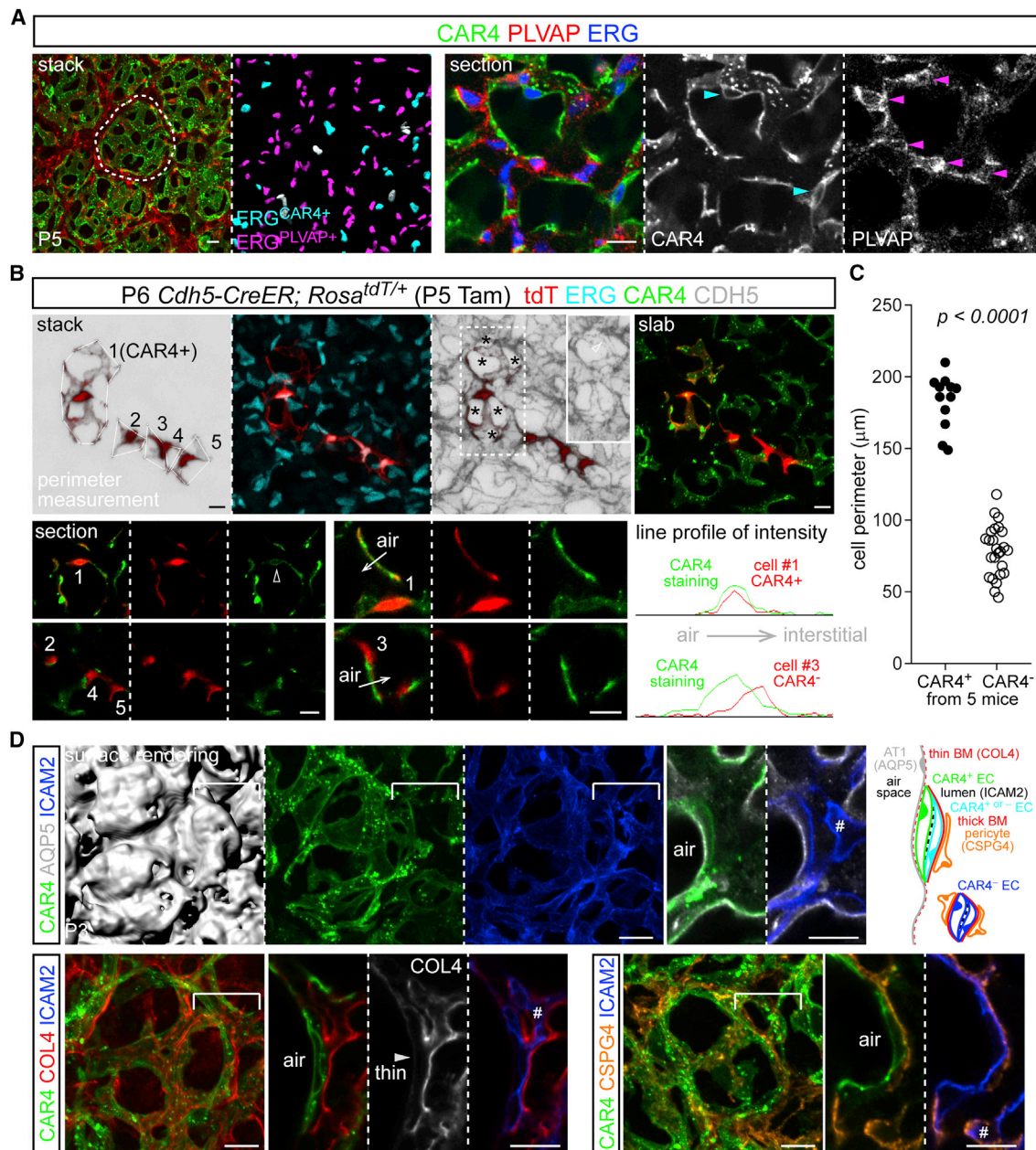
Figure 5. Car4 ECs Localize to the Alveolar Islands and Have an Expansive Morphology

(A) Representative en face stack view and section view of whole-mount immunostained lungs from at least 5 mice. CAR4 staining covers whereas PLVAP staining surrounds alveolar islands (dash). Perinuclear CAR4 and PLVAP staining allows assignment of ERG nuclei to CAR4 (cyan arrowhead) versus PLVAP (magenta arrowhead) ECs; gray nuclei are ambiguous.

(B) Whole-mount immunostaining of lungs with sparsely labeled ECs, representative of at least 5 mice, viewed as an en face stack view (40 μm), slab view (20 μm), or section view (1 μm). Accumulation of tdT to ERG nuclei allows cell numeration: cell #1 is a Car4 EC and cells #2–5 are non-Car4 ECs. Asterisk, avascular tissue surrounded by a single net-like Car4 EC. Boxed region is shown for CDH5 single staining as an inset to show a CDH5 junction (open arrowhead) overlapping with a single Car4 EC. Cell perimeter is measured by connecting protrusions that are visible in a projection view. Line profile analysis shows aligned versus shifted peaks for Car4 versus non-Car4 ECs, respectively. For shifted peaks, Car4 ECs are closer to the air space than non-Car4 ECs (e.g., cell #3). Tam, 0.25 μg tamoxifen.

(C) Quantification of cell perimeter and comparison using Student's t test. Each symbol represents one cell.

(D) En face stack view and associated section view of the "slope" of alveolar islands (bracket) of whole-mount immunostained lungs, representative of at least 5 mice. As in the color-matched diagram, Car4 ECs (green) are closer to the air space (AQP5; gray) than non-Car4 ECs (blue), lined by a thin basement membrane (BM) (COL4, red) without intervening pericytes (CSPG4, orange). #, non-CAR4 ECs.

Scale bars, 10 μm.

See also Figure S5.
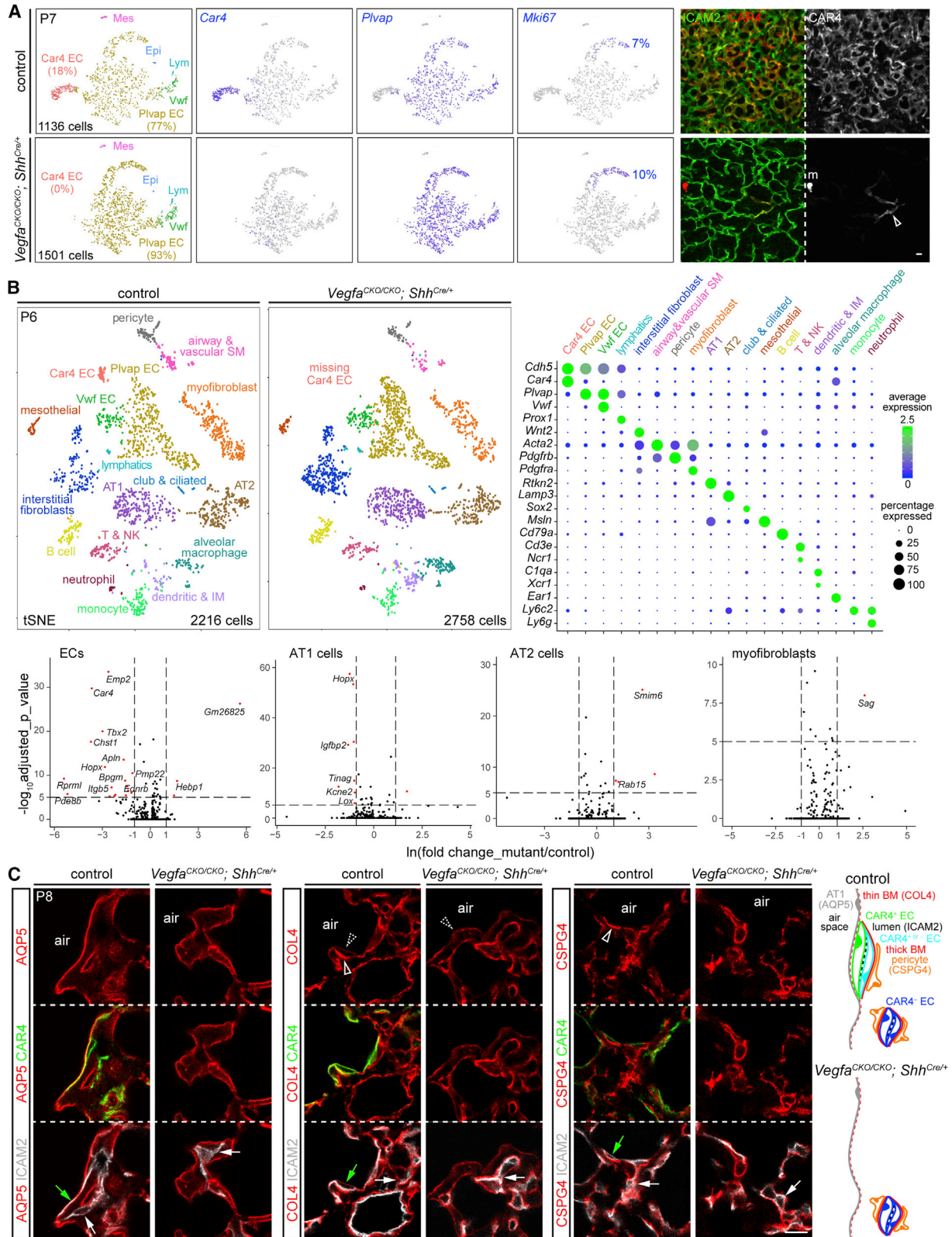
Figure 6. Car4 ECs Are Specifically Lost upon Pan-epithelial *Vegfa* Deletion

(A) Left: tSNE plots of scRNA-seq of sorted ECs from littermate lungs showing a specific, complete loss of Car4 ECs in the mutant with the population percentages in parenthesis. Plvap ECs and proliferating (*Mki67*) ECs are unaffected. Cell populations are color coded as in Figures 3 and 4. Mes, mesenchyme; Epi, epithelium;

(Figure S5A). In the central retina, ECs either were elongated along large vessels, similar to those in non-capillaries of the lung, or had a limited number of projections, similar to the lung Plvap ECs. In the peripheral retina, tip ECs displayed their characteristic blind-end filopodia, which were never found in the lung. Conversely, the expansive net-like morphology of Car4 ECs of the lung was also never found in the retina (Figure S5A).

Among the tip EC genes shared by the lung Car4 ECs, we focused on *Apln* because of its reported role in sprouting angiogenesis (del Toro et al., 2010) and its receptor *Aplnr* was specific to Plvap ECs (Figure 3). Using an $Apln^{CreER}$ knockin, knockout allele (Liu et al., 2015), we found that *Apln* underwent X-inactivation and, when tested with a $Rosa^{L10GFP}$ reporter, recombination was variable and enriched in but not specific to Car4 ECs (Figures S6A and S6B). In addition, scRNA-seq comparison of sorted lung ECs from mutant ($Apln^{CreER/Y}$) and littermate control males showed, as expected, a complete loss of *Apln* specifically in Car4 ECs but no difference in either the number or gene expression of Car4 and Plvap ECs (Figure S6C). Therefore, despite their intriguing expression patterns, the functional relevance of *Apln* and *Aplnr* in the lung is uncertain.

Taken together, the cross-organ comparison identified similarities and differences in EC gene expression and cell morphology, suggesting a common core vascular pathway superimposed with organ-specific adaptation.

CAR4 ECs Are Specifically Lost upon Epithelial Vegfa Deletion

Given their similarity to the retina tip ECs, which require VEGFA (Gerhardt et al., 2003), we asked if Car4 ECs of the lung also depended on VEGFA. To test this, we performed scRNA-seq on sorted ECs from control and pan-epithelial *Vegfa* mutant lungs. Remarkably, the mutant lung specifically and completely lost the Car4 EC population, which represented 18% of all ECs in the control lung (Figure 6A). In comparison, Plvap, Vwf, and lymphatic ECs were unaffected and proliferating ECs—marked by *Mki67* and frequent in early post-natal lungs—were also unaffected, which was consistent with our immunostaining-based quantification (Figures 6 and 2B). This specific loss of Car4 ECs was confirmed by immunostaining, showing that, in the mutant lung, CAR4 was rarely detected in the remaining vessels but unaffected in alveolar macrophages where CAR4 was normally present (Figure 6A).

To extend our analysis to non-ECs, we performed scRNA-seq on another pair of control and pan-epithelial *Vegfa* mutant lungs that were sorted into epithelial, endothelial, immune, and mesenchymal cell lineages using ECAD, ICAM2, and CD45 antibodies and then sequenced in equal proportions (Figure S3D). All major lung cell types were readily identifiable by their known markers (Figure 6B). Car4 ECs were again completely missing in the mutant, resulting in downregulation of the aforementioned Car4-EC markers (Figure 6B). Other cell types, including AT2 and myofibroblasts, were largely unaffected transcriptionally except for a small decrease in several markers in AT1 cells, possibly reflecting a minor differentiation delay in the absence of adjacent Car4 ECs (Figure 6B). This extended analysis confirmed the specificity of the requirement of VEGFA for Car4 ECs. Our all-inclusive gating strategy (Figure S3D) also validated our EC classifications (Figure 3).

The specific, complete loss of Car4 ECs in the pan-epithelial *Vegfa* mutant allowed confirmation of our prior spatial characterization of Car4 ECs (Figure 5D). Indeed, CAR4$^+$ ECs—those that expressed CAR4 in the control but were absent in the *Vegfa* mutant—abutted the AT1 cell membrane and shared a thin basement membrane with the epithelium without intervening pericytes (Figure 6C). In contrast, CAR4$^-$ ECs—those that did not express CAR4 in the control but comprised all remaining vessels in the mutant—were away from the AT1 cell membrane, underlain with a thicker basement membrane and surrounded by pericyte processes (Figure 6C). For vessels abutting the AT1 cell membrane, the side further away from the air space could consist of CAR4$^-$ ECs, as described in Figure 5B, and were found to be covered by a thicker basement membrane and pericyte processes (Figures 5D, 6C, and the diagrams herein). Without Car4 ECs, as in the pan-epithelial *Vegfa* mutant, the CAR4$^-$ ECs in such hybrid vessels were also missing in the aforementioned secondary septae of the alveolar islands (Figures 2A and 6A) and therefore depended on CAR4$^+$ ECs for such locations, reminiscent of stalk ECs depending on tip ECs to spread to avascular regions.

The co-development of Car4 ECs and *Vegfa*-expressing AT1 cells and the requirement of VEGFA in forming Car4 ECs prompted us to test if VEGFA was sufficient to induce Car4 ECs from purified primary lung ECs in culture (Wang et al., 2019) (Figure S7A). Although there was a trend of increased Car4 ECs upon VEGFA treatment, less than 0.5% ECs expressed CAR4, suggesting that conventional EC cultures did not recapitulate *in vivo* conditions, such as contact with AT1 cells and blood flow.

Lym, lymphatic EC; Vwf, Vwf EC. Compared to P14 (Figure 3), P7 lungs have more proliferating (*Mki67*) ECs; their percentage is calculated with a UMI cutoff of 1. Right: en face view of immunostained lungs, representative of at least 3 littermate pairs, showing rare Car4 staining in the remaining vessels in the mutant (open arrowhead). m, macrophage.

(B) tSNE plots of scRNA-seq of 4 sorted cell lineages from littermate lungs: epithelial, endothelial, mesenchymal, and immune. Dot plot showing markers for the color-coded cell types. Car4 ECs are missing in the mutant. Volcano plots comparing all ECs, AT1 cells, AT2 cells, and myofibroblasts between control and mutant show downregulation of markers for Car4 ECs and minor changes in other cell types. SM, smooth muscle; T & NK, T and NK cells; IM, interstitial macrophages.

(C) Section immunostaining images of lungs, representative of at least 3 littermate pairs. As diagrammed, Car4 vessels (filled green arrow) abut the epithelium (AQP5), separated by a thin basement membrane (BM) (weak COL4 staining, dash open arrowhead) with no intervening pericytes (CSPG4, dash open arrowhead), but their sides away from the air space have a thicker basement membrane (strong COL4 staining, solid open arrowhead) and pericytes (solid open arrowhead). Non-Car4 vessels (filled white arrow, a subset of vessels in the control and all vessels in the mutant) do not abut the epithelium and are surrounded by a thick basement membrane and pericytes.

Scale bars, 10 μm.

See also Figure S7.
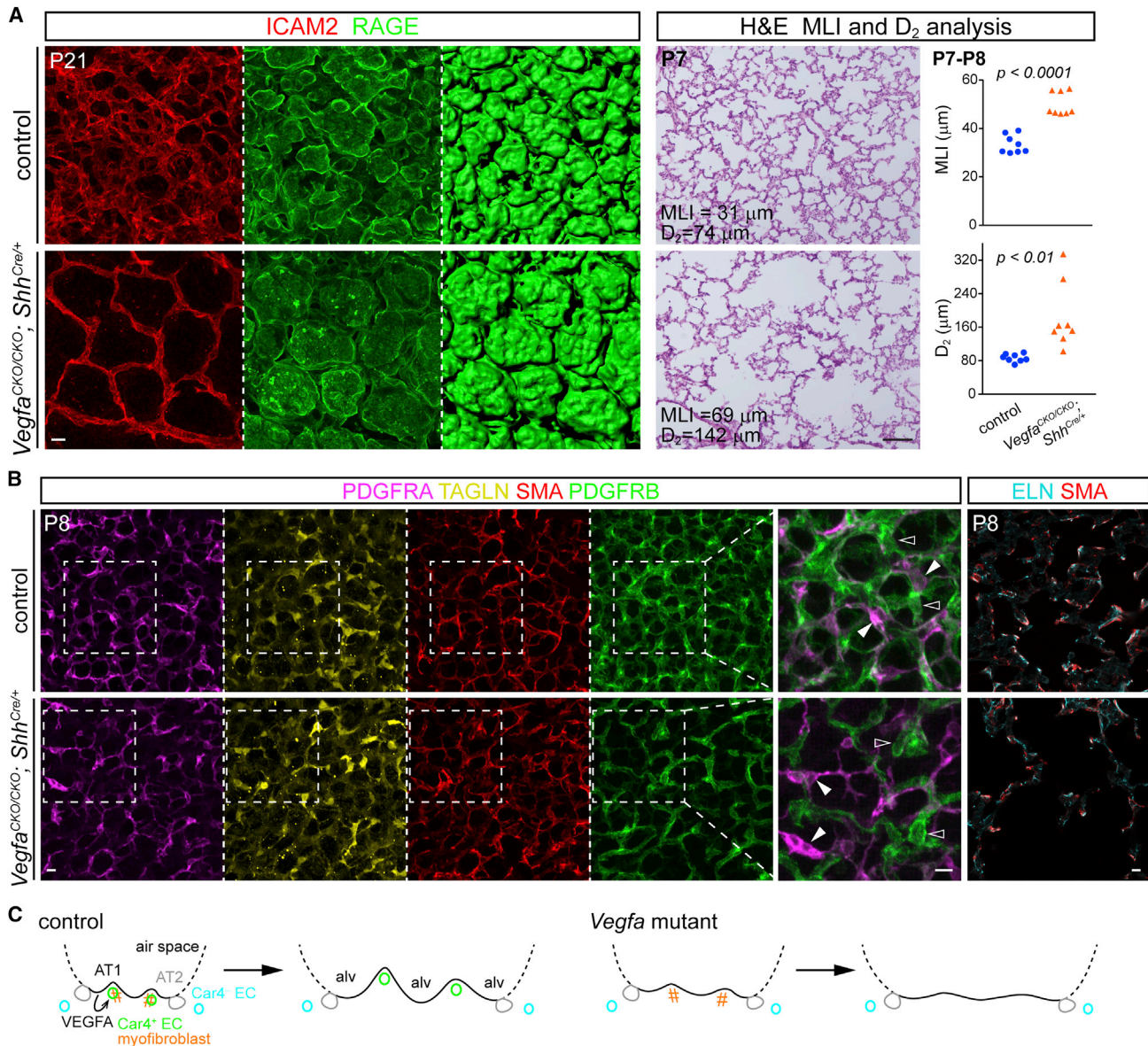
Figure 7. Aberrant Alveolar Enlargement in the Absence of Car4 ECs but Independent of Myofibroblasts

(A) Left: en face view of immunostained lungs, representative of at least 3 littermate pairs, showing a smoother surface (RAGE) of alveolar islands that are not subdivided by Car4 vessels in the mutant. Right: H&E section images of littermate lungs with the corresponding mean linear intercept (MLI) and D_2 measurements. Each symbol represents 1 mouse and is the average of 3 regions (Student's t test).

(B) Left: en face view of immunostained lungs, representative of at least 3 littermate pairs, showing fewer pericytes (PDGFRB, open arrowhead) but normal myofibroblasts (PDGFRA-TAGLN-SMA triple positive, although variable in staining intensity, filled arrowhead) in the mutant. Boxed regions are magnified. Right: section immunostaining showing colocalization of elastin (ELN) with SMA.

(C) Schematics with color-coded cell types showing AT1-derived VEGFA signals to Car4 ECs, which, together with myofibroblasts, promote secondary septation and persist in the resulting septae even after disappearance of myofibroblasts in the mature lung. The pan-epithelial *Vegfa* mutant fails to form Car4 ECs and non-Car4 ECs and myofibroblasts are insufficient for secondary septation, resulting in alveolar enlargement. Note that Car4 vessels may consist of Car4 ECs and non-Car4 ECs, as diagrammed in Figure 6C. Alv, alveolus.

Scale bars, 10 μm except for H&E images (where scale bars, 100 μm).

See also Figure S7.

CAR4 ECs Contribute to Alveolar Morphogenesis Independent of Myofibroblasts

The existence of CAR4^{+} vessels in secondary septation and their specific absence in the pan-epithelial *Vegfa* mutant (Figures 1D, 2A, and 6A) led us to examine the role of Car4 ECs in alveolar morphogenesis. Indeed, without the CAR4^{+} vessels coursing through the previously described grooves of the folding AT1 cells, the AT1 surface was smoother in the mutant (Figures 2A and 7A). Consistent with a failure in secondary septation, the air space in the mutant lung was aberrantly enlarged, as

CellPress

quantified using a mean linear intercept (MLI) method (Liu et al., 2017) as well as a D_2 method that measured area-weighted air space diameters and bypassed the difficulty in distinguishing alveolar ducts and alveoli in the mouse lung (Jacob et al., 2009; Massaro and Massaro, 1996; Parameswaran et al., 2006) (Figure 7A). Air space enlargement was more variable in the AT1-specific *Vegfa* mutant, possibly due to delayed or incomplete *Vegfa* deletion (Figure S7B).

Defective alveologenesis in the pan-epithelial *Vegfa* mutant occurred despite the normal specification and localization of myofibroblasts, a widely accepted driver of secondary septation (Boström et al., 1996) (Figures 2A, 7B, and S2C). We further examined the mesenchymal lineage using a 4-marker panel: PDGFRA, SMA, TAGLN (also known as SM22), and PDGFRB (Figure 7B). The perinuclear accumulation of PDGFRA, PDGFRB, and TAGLN allowed colocalization and assignment of cell types, while the commonly used myofibroblast marker SMA was not useful for such application but largely matched the cytoplasmic TAGLN staining. PDGFRB-expressing pericytes were distinct from PDGFRA cells, which expressed TAGLN and SMA and were thereby considered myofibroblasts. The mutant lung had fewer PDGFRB pericytes presumably as a result of loss of CAR4$^+$ capillaries, but the PDGFRA-TAGLN-SMA-expressing myofibroblasts were unaffected and elastin still colocalized with SMA (Figure 7B). These data are consistent with the notion that Car4 ECs, possibly together with the associated pericytes but independent of myofibroblasts, are required for alveolar morphogenesis.

DISCUSSION

In this study, we show that the pulmonary microvasculature is heterogeneous and harbors a transcriptionally distinct EC population that is defined by CAR4 expression and specifically requires epithelial-derived VEGFA, which is predominantly supplied by AT1 cells. These Car4 ECs feature an extended net-like morphology, situate seamlessly over the alveolar epithelium and specifically in regions undergoing secondary septation, and are required for alveolar morphogenesis independent of myofibroblasts (Figure 7C). This work opens another avenue of vascular research and has implications in alveolar development, physiology, and pathogenesis.

Our study reveals remarkable parallels between retinal tip ECs and lung Car4 ECs: (1) retinal astrocytes express *Vegfa* and provide the scaffold for tip ECs (Gariano and Gardner, 2005), whereas lung AT1 cells express *Vegfa* and provide the surface for Car4 ECs and (2) VEGFA in the retina induces tip ECs with characteristic filopodia and tip EC genes, whereas VEGFA in the lung induces Car4 ECs with characteristic net-like morphology and a subset of retina tip EC genes, such as Apln. However, there are also substantial differences: (1) the retina vasculature undergoes sprouting angiogenesis to spread from the central vascularized region to the peripheral avascular region in response to a hypoxia-induced VEGFA gradient, whereas the post-natal lung vasculature is surrounded by inhaled oxygen, always covers the alveolar epithelium as a dense net, and is believed to undergo intussusceptive angiogenesis (Burri et al., 2004) to match the expansion of the epithelial surface and (2) tip ECs disappear after development, but Car4 ECs persist even in the mature lung (Figure S6C). Future mecha-

nistic dissection of the common and distinct signaling events downstream of VEGFA in the two organs should shed light on the poorly understood process of intussusceptive angiogenesis and may establish lung Car4 ECs as another model for vascular biology. More broadly, understanding organ-specific function of *Vegfa* may pave the way for targeted anti-VEGF therapy (Meadows and Hurwitz, 2012).

Alveologenesis, formation of alveoli, divides primary alveolar sacs—resulting from expansion of embryonic branch tips—into mature alveoli via the process of secondary septation (Yang and Chen, 2014). These secondary septae are marked by myofibroblasts, SMA-expressing contractile mesenchymal cells. Notably, we previously showed that such SMA-marked septae are the grooves of folded AT1 cells and coincide with capillaries that, as shown in this study, are composed of Car4 ECs. Furthermore, although myofibroblasts are required for secondary septation in response to PDGFA signaling (Boström et al., 1996; Li et al., 2018b), our pan-epithelial *Vegfa* mutant is missing Car4 ECs without affecting myofibroblasts or PDGFRA expression and yet displays aberrantly enlarged alveoli—consistent with a failure in secondary septation. This result raises the possibility that the force-generating myofibroblasts initiate secondary septation and AT1 cell folding, which is stabilized and maintained by CAR4$^+$ vessels or their associated pericytes (Kato et al., 2018). This possibility is also consistent with the observation that myofibroblasts disappear or adopt other cell fates after the lung matures, whereas the vasculature persists (Li et al., 2018b; Yang et al., 2016). On the other hand, the remaining vessels around the alveolar islands in the *Vegfa* mutant will still constrain alveolar expansion; these vessels are normally also associated with myofibroblasts such that a myofibroblast deficiency should lead to more severe alveolar simplification. In addition, the unaffected myofibroblasts both on and around the alveolar islands in the *Vegfa* mutant may ameliorate the alveologenesis phenotype. Future work will examine Car4 ECs in mutants that directly affect myofibroblasts and examine both myofibroblasts and Car4 ECs in experimental BPD models and patients with BPD, which is characterized by defective alveologenesis (Abman, 2001).

Car4 ECs are likely to have additional functions beyond alveologenesis. First, compared to other ECs, Car4 ECs co-develop with the gas-exchanging AT1 cells, have a larger surface area, and are located closest to the alveolar epithelium, separated by a thinner basement membrane without intervening pericytes—all features suggesting a high efficiency in gas exchange. Testing this would require monitoring gas exchange in Car4$^+$ versus CAR4$^-$ capillaries because conventional blood gas measurement of the *Vegfa* mutant will not distinguish a general loss of capillaries from a specific loss of high-efficiency Car4$^+$ capillaries. Second, Car4 ECs specifically express secreted ligands including *Apln* and *Kitl* while the corresponding receptors, *Aplnr* and *Kit*, are expressed by Plvap ECs, suggesting possible signaling roles of Car4 ECs toward other ECs. However, our examination of the *Apln* mutant does not revealed any vascular phenotype. Future studies should focus on Car4-EC-specific genes, including CAR4 itself, which intriguingly is an enzyme involved in carbon dioxide formation (Crandall and O'Brasky, 1978; Fleming et al., 1993). Finally, the persistence of Car4 ECs in the mature lung calls for a better understanding of their role in homeostasis and injury repair.

CellPress

STAR★METHODS

Detailed methods are provided in the online version of this paper and include the following:

- KEY RESOURCES TABLE
- LEAD CONTACT AND MATERIALS AVAILABILITY
- EXPERIMENTAL MODEL AND SUBJECT DETAILS
  - Mice (*Mus musculus*)
- METHOD DETAILS
  - Antibodies
  - Section Immunostaining
  - Wholemount Immunostaining
  - Section *In Situ* Hybridization
  - Western Blot
  - Vasculature Analysis
  - D$_2$ Air Space Analysis and Mean Linear Intercept (MLI) Analysis
  - Cell Dissociation and FACS
  - RT-PCR and Bulk RNA-Seq
  - Single-Cell RNA-Seq
  - Primary EC culture
- QUANTIFICATION AND STATISTICAL ANALYSIS
- DATA AND CODE AVAILABILITY

SUPPLEMENTAL INFORMATION

Supplemental Information can be found online at https://doi.org/10.1016/j.devcel.2020.01.009.

AUTHOR CONTRIBUTIONS

L.V.E., J.D.W., and J.C. designed the research; L.V.E., M.P.C., V.H., E.J.O., and J.C. performed the research; P.F., E.D.C., and Z.B. provided the *Aqp5^Cre* mice; B.Z. provided the *Apln^CreER* mice; L.V.E., J.D.W., and J.C. wrote the paper; and all authors read and approved the paper.

DECLARATION OF INTERESTS

The authors declare no competing interests.

REFERENCES

Abman, S.H. (2001). Bronchopulmonary dysplasia: "a vascular hypothesis". Am. J. Respir. Crit. Care Med. *164*, 1755–1756.

Aird, W.C. (2007a). Phenotypic heterogeneity of the endothelium: I. Structure, function, and mechanisms. Circ. Res. *100*, 158–173.

Aird, W.C. (2007b). Phenotypic heterogeneity of the endothelium: II. Representative vascular beds. Circ. Res. *100*, 174–190.

Alanis, D.M., Chang, D.R., Akiyama, H., Krasnow, M.A., and Chen, J. (2014). Two nested developmental waves demarcate a compartment boundary in the mouse lung. Nat. Commun. *5*, 3923.

Barkauskas, C.E., Cronce, M.J., Rackley, C.R., Bowie, E.J., Keene, D.R., Stripp, B.R., Randell, S.H., Noble, P.W., and Hogan, B.L. (2013). Type 2 alveolar cells are stem cells in adult lung. J. Clin. Invest. *123*, 3025–3036.

Blanco, R., and Gerhardt, H. (2013). VEGF and Notch in tip and stalk cell selection. Cold Spring Harbor Perspect. Med. *3*, a006569.

Blighe, K., Rana, S., and Lewis, M. (2019). EnhancedVolcano: Publication-ready volcano plots with enhanced colouring and labeling. R package version 1.4.0. https://github.com/kevinblighe/EnhancedVolcano.

Boström, H., Willetts, K., Pekny, M., Levéen, P., Lindahl, P., Hedstrand, H., Pekna, M., Hellström, M., Gebre-Medhin, S., Schalling, M., et al. (1996). PDGF-A signaling is a critical event in lung alveolar myofibroblast development and alveogenesis. Cell *85*, 863–873.

Burri, P.H., Hlushchuk, R., and Djonov, V. (2004). Intussusceptive angiogenesis: its emergence, its characteristics, and its significance. Dev. Dyn. *231*, 474–488.

Butler, A., Hoffman, P., Smibert, P., Papalexi, E., and Satija, R. (2018). Integrating single-cell transcriptomic data across different conditions, technologies, and species. Nat. Biotechnol. *36*, 411–420.

Chang, D.R., Martinez Alanis, D., Miller, R.K., Ji, H., Akiyama, H., McCrea, P.D., and Chen, J. (2013). Lung epithelial branching program antagonizes alveolar differentiation. Proc. Natl. Acad. Sci. USA *110*, 18042–18051.

Crandall, E.D., and O'Brasky, J.E. (1978). Direct evidence of participation of rat lung carbonic anhydrase in CO$_2$ reactions. J. Clin. Invest. *62*, 618–622.

Dejana, E., Hirschi, K.K., and Simons, M. (2017). The molecular basis of endothelial cell plasticity. Nat. Commun. *8*, 14361.

del Toro, R., Prahst, C., Mathivet, T., Siegfried, G., Kaminker, J.S., Larrivee, B., Breant, C., Duarte, A., Takakura, N., Fukamizu, A., et al. (2010). Identification and functional analysis of endothelial tip cell-enriched genes. Blood *116*, 4025–4033.

Desai, T.J., Brownfield, D.G., and Krasnow, M.A. (2014). Alveolar progenitor and stem cells in lung development, renewal and cancer. Nature *507*, 190–194.

Durr, E., Yu, J., Krasinska, K.M., Carver, L.A., Yates, J.R., Testa, J.E., Oh, P., and Schnitzer, J.E. (2004). Direct proteomic mapping of the lung microvascular endothelial cell surface in vivo and in cell culture. Nat. Biotechnol. *22*, 985–992.

Fish, J.E., Cantu Gutierrez, M., Dang, L.T., Khyzha, N., Chen, Z., Veitch, S., Cheng, H.S., Khor, M., Antounians, L., Njock, M.S., et al. (2017). Dynamic regulation of VEGF-inducible genes by an ERK/ERG/p300 transcriptional network. Development *144*, 2428–2444.

Fleming, R.E., Crouch, E.C., Ruzicka, C.A., and Sly, W.S. (1993). Pulmonary carbonic anhydrase IV: developmental regulation and cell-specific expression in the capillary endothelium. Am. J. Physiol. *265*, L627–L635.

Flodby, P., Borok, Z., Banfalvi, A., Zhou, B., Gao, D., Minoo, P., Ann, D.K., Morrisey, E.E., and Crandall, E.D. (2010). Directed expression of Cre in alveolar epithelial type 1 cells. Am. J. Respir. Cell Mol. Biol. *43*, 173–178.

Gariano, R.F., and Gardner, T.W. (2005). Retinal angiogenesis in development and disease. Nature *438*, 960–966.

Gerber, H.P., Hillan, K.J., Ryan, A.M., Kowalski, J., Keller, G.A., Rangell, L., Wright, B.D., Radtke, F., Aguet, M., and Ferrara, N. (1999). VEGF is required for growth and survival in neonatal mice. Development *126*, 1149–1159.

Gerhardt, H., Golding, M., Fruttiger, M., Ruhrberg, C., Lundkvist, A., Abramsson, A., Jeltsch, M., Mitchell, C., Alitalo, K., Shima, D., et al. (2003). VEGF guides angiogenic sprouting utilizing endothelial tip cell filopodia. J. Cell Biol. *161*, 1163–1177.

Han, X., Wang, R., Zhou, Y., Fei, L., Sun, H., Lai, S., Saadatpour, A., Zhou, Z., Chen, H., Ye, F., et al. (2018). Mapping the mouse cell atlas by microwell-seq. Cell *172*, 1091–1107.e17.

Harfe, B.D., Scherz, P.J., Nissim, S., Tian, H., McMahon, A.P., and Tabin, C.J. (2004). Evidence for an expansion-based temporal Shh gradient in specifying vertebrate digit identities. Cell 118, 517–528.

Harris, K.S., Zhang, Z., McManus, M.T., Harfe, B.D., and Sun, X. (2006). Dicer function is essential for lung epithelium morphogenesis. Proc. Natl. Acad. Sci. USA 103, 2208–2213.

Jacob, R.E., Carson, J.P., Gideon, K.M., Amidan, B.G., Smith, C.L., and Lee, K.M. (2009). Comparison of two quantitative methods of discerning airspace enlargement in smoke-exposed mice. PLoS One 4, e6670.

Kato, K., Diéguez-Hurtado, R., Park, D.Y., Hong, S.P., Kato-Azuma, S., Adams, S., Stehling, M., Trappmann, B., Wrana, J.L., Koh, G.Y., and Adams, R.H. (2018). Pulmonary pericytes regulate lung morphogenesis. Nat. Commun. 9, 2448.

Kim, D., Pertea, G., Trapnell, C., Pimentel, H., Kelley, R., and Salzberg, S.L. (2013). TopHat2: accurate alignment of transcriptomes in the presence of insertions, deletions and gene fusions. Genome Biol. 14, R36.

Langmead, B., and Salzberg, S.L. (2012). Fast gapped-read alignment with Bowtie 2. Nat. Methods 9, 357–359.

Lavin, Y., Winter, D., Blecher-Gonen, R., David, E., Keren-Shaul, H., Merad, M., Jung, S., and Amit, I. (2014). Tissue-resident macrophage enhancer landscapes are shaped by the local microenvironment. Cell 159, 1312–1326.

Li, J., Wang, Z., Chu, Q., Jiang, K., Li, J., and Tang, N. (2018a). The strength of mechanical forces determines the differentiation of alveolar epithelial cells. Dev. Cell 44, 297–312.e5.

Li, R., Bernau, K., Sandbo, N., Gu, J., Preissl, S., and Sun, X. (2018b). Pdgfra marks a cellular lineage with distinct contributions to myofibroblasts in lung maturation and injury response. eLife 7, e36865.

Little, D.R., Gerner-Mauro, K.N., Flodby, P., Crandall, E.D., Borok, Z., Akiyama, H., Kimura, S., Ostrin, E.J., and Chen, J. (2019). Transcriptional control of lung alveolar type 1 cell development and maintenance by NK homeobox 2–1. Proc. Natl. Acad. Sci. USA 116, 20545–20555.

Liu, J., Krautzberger, A.M., Sui, S.H., Hofmann, O.M., Chen, Y., Baetscher, M., Grgic, I., Kumar, S., Humphreys, B.D., Hide, W.A., and McMahon, A.P. (2014). Cell-specific translational profiling in acute kidney injury. J. Clin. Invest. 124, 1242–1254.

Liu, Q., Hu, T., He, L., Huang, X., Tian, X., Zhang, H., He, L., Pu, W., Zhang, L., Sun, H., et al. (2015). Genetic targeting of sprouting angiogenesis using Apln-CreER. Nat. Commun. 6, 6020.

Liu, Z., Fu, S., and Tang, N. (2017). A standardized method for measuring internal lung surface area via mouse pneumonectomy and prosthesis implantation. J. Vis. Exp. 125, 56114.

Madisen, L., Zwingman, T.A., Sunkin, S.M., Oh, S.W., Zariwala, H.A., Gu, H., Ng, L.L., Palmiter, R.D., Hawrylycz, M.J., Jones, A.R., et al. (2010). A robust and high-throughput Cre reporting and characterization system for the whole mouse brain. Nat. Neurosci. 13, 133–140.

Massaro, G.D., and Massaro, D. (1996). Formation of pulmonary alveoli and gas-exchange surface area: quantitation and regulation. Annu. Rev. Physiol. 58, 73–92.

Meadows, K.L., and Hurwitz, H.I. (2012). Anti-VEGF therapies in the clinic. Cold Spring Harbor Perspect. Med. 2, a006577.

Miquerol, L., Gertsenstein, M., Harpal, K., Rossant, J., and Nagy, A. (1999). Multiple developmental roles of VEGF suggested by a LacZ-tagged allele. Dev. Biol. 212, 307–322.

Morrisey, E.E., and Hogan, B.L. (2010). Preparing for the first breath: genetic and cellular mechanisms in lung development. Dev. Cell 18, 8–23.

Muzumdar, M.D., Tasic, B., Miyamichi, K., Li, L., and Luo, L. (2007). A global double-fluorescent Cre reporter mouse. Genesis 45, 593–605.

Parameswaran, H., Majumdar, A., Ito, S., Alencar, A.M., and Suki, B. (2006). Quantitative characterization of airspace enlargement in emphysema. J. Appl. Physiol. 100, 186–193.

Potente, M., and Mäkinen, T. (2017). Vascular heterogeneity and specialization in development and disease. Nat. Rev. Mol. Cell Biol. 18, 477–494.

Qiu, X., Mao, Q., Tang, Y., Wang, L., Chawla, R., Pliner, H.A., and Trapnell, C. (2017). Reversed graph embedding resolves complex single-cell trajectories. Nat. Methods 14, 979–982.

Roberts, A., Pimentel, H., Trapnell, C., and Pachter, L. (2011a). Identification of novel transcripts in annotated genomes using RNA-Seq. Bioinformatics 27, 2325–2329.

Roberts, A., Trapnell, C., Donaghey, J., Rinn, J.L., and Pachter, L. (2011b). Improving RNA-Seq expression estimates by correcting for fragment bias. Genome Biol. 12, R22.

Rocha, S.F., Schiller, M., Jing, D., Li, H., Butz, S., Vestweber, D., Biljes, D., Drexler, H.C., Nieminen-Kelhä, M., Vajkoczy, P., et al. (2014). Esm1 modulates endothelial tip cell behavior and vascular permeability by enhancing VEGF bioavailability. Circ. Res. 115, 581–590.

Sabbagh, M.F., Heng, J.S., Luo, C., Castanon, R.G., Nery, J.R., Rattner, A., Goff, L.A., Ecker, J.R., and Nathans, J. (2018). Transcriptional and epigenomic landscapes of CNS and non-CNS vascular endothelial cells. eLife 7, e36187.

Shah, A.V., Birdsey, G.M., and Randi, A.M. (2016). Regulation of endothelial homeostasis, vascular development and angiogenesis by the transcription factor ERG. Vascul. Pharmacol. 86, 3–13.

Stevens, T., Phan, S., Frid, M.G., Alvarez, D., Herzog, E., and Stenmark, K.R. (2008). Lung vascular cell heterogeneity: endothelium, smooth muscle, and fibroblasts. Proc. Am. Thorac. Soc. 5, 783–791.

Takeda, N., Jain, R., LeBoeuf, M.R., Wang, Q., Lu, M.M., and Epstein, J.A. (2011). Interconversion between intestinal stem cell populations in distinct niches. Science 334, 1420–1424.

Thébaud, B., and Abman, S.H. (2007). Bronchopulmonary dysplasia: where have all the vessels gone? Roles of angiogenic growth factors in chronic lung disease. Am. J. Respir. Crit. Care Med. 175, 978–985.

Trapnell, C., Cacchiarelli, D., Grimsby, J., Pokharel, P., Li, S., Morse, M., Lennon, N.J., Livak, K.J., Mikkelsen, T.S., and Rinn, J.L. (2014). The dynamics and regulators of cell fate decisions are revealed by pseudotemporal ordering of single cells. Nat. Biotechnol. 32, 381–386.

Trapnell, C., Hendrickson, D.G., Sauvageau, M., Goff, L., Rinn, J.L., and Pachter, L. (2013). Differential analysis of gene regulation at transcript resolution with RNA-seq. Nat. Biotechnol. 31, 46–53.

Trapnell, C., Roberts, A., Goff, L., Pertea, G., Kim, D., Kelley, D.R., Pimentel, H., Salzberg, S.L., Rinn, J.L., and Pachter, L. (2012). Differential gene and transcript expression analysis of RNA-seq experiments with TopHat and Cufflinks. Nat. Protoc. 7, 562–578.

Wang, J., Niu, N., Xu, S., and Jin, Z.G. (2019). A simple protocol for isolating mouse lung endothelial cells. Sci. Rep. 9, 1458.

Wang, Y., Nakayama, M., Pitulescu, M.E., Schmidt, T.S., Bochenek, M.L., Sakakibara, A., Adams, S., Davy, A., Deutsch, U., Lüthi, U., et al. (2010). Ephrin-B2 controls VEGF-induced angiogenesis and lymphangiogenesis. Nature 465, 483–486.

Yamamoto, H., Yun, E.J., Gerber, H.P., Ferrara, N., Whitsett, J.A., and Vu, T.H. (2007). Epithelial-vascular cross talk mediated by VEGF-A and HGF signaling directs primary septae formation during distal lung morphogenesis. Dev. Biol. 308, 44–53.

Yang, J., and Chen, J. (2014). Developmental programs of lung epithelial progenitors: a balanced progenitor model. Wiley Interdiscip. Rev. Dev. Biol. 3, 331–347.

Yang, J., Hernandez, B.J., Martinez Alanis, D., Narvaez del Pilar, O., Vila-Ellis, L., Akiyama, H., Evans, S.E., Ostrin, E.J., and Chen, J. (2016). The development and plasticity of alveolar type 1 cells. Development 143, 54–65.

STAR★METHODS

KEY RESOURCES TABLE

REAGENT or RESOURCE	SOURCE	IDENTIFIER
Antibodies		
BV786 Rat Anti-Mouse CD31	BD Biosciences	740870
Purified Rat Anti-Mouse CD31 (MEC 13.3)	BD Biosciences	550274
PE/Cy7 anti-mouse CD45	BioLegend	103114
ICAM-2 Monoclonal Antibody (3C4), Alexa Fluor 647	ThermoFisher	A15452
Goat anti-mouse Carbonic Anhydrase IV/CA4 Antibody	R&D	AF2414
Chicken Anti-GFP	Abcam	AB13970
CD102 (ICAM-2) Monoclonal Antibody (3C4 (mIC2 / 4))	eBioscience	16-1021-82
Goat anti-mouse ICAM-2/CD102 Antibody	R&D systems	AF774
Rabbit anti-Histone H3 (H3)	Cell Signaling	4499
Goat anti-rabbit IgG HRP-linked	Cell Signaling	7074
Rabbit anti-Aquaporin 5	Abcam	ab78486
CD324 (E-Cadherin) Monoclonal Antibody (DECMA-1), Alexa Fluor 488	eBioscience	53-3249-80
Anti-Actin, α-Smooth Muscle - Cy3™ antibody, Mouse monoclonal	Sigma Aldrich	C6198
Ki-67 Monoclonal Antibody (SolA15), eFluor 570	eBioscience	41-5698-82
Ki-67, Rabbit Monoclonal Antibody	ThermoFisher	RM9106S0
Rat anti-endomucin	eBioscience	14-5851-81
Rabbit anti-ERG	Abcam	ab92513
Goat anti-ESM1	R&D systems	AF1999
Goat anti-Elastin	Dr. Barry Starcher	n/a
Anti-Collagen 4 pAb (Mouse)	CosmoBioUSA	LSL-LB-1403
Anti-NG2 Chondroitin Sulfate Proteoglycan Antibody	Millipore	AB5320
Rat anti-Plvap	BD Biosciences	553849
Rabbit Polyclonal RFP Antibody	Rockland	600-401-379
Alexa Fluor 647 Rat Anti-Mouse CD144	BD Biosciences	562242
Mouse PDGF R beta Antibody	R&D systems	AF1042
CD140a (PDGFRA) Monoclonal Antibody (APA5)	eBioscience	14-1401-82
Rat anti-RAGE Antibody	R&D systems	MAB1179
Rabbit anti-Prox1	AngioBio	11-002
Mouse Endocan/ESM-1 Antibody	R&D	AF1999
Mouse DLL4 Antibody	R&D	AF1389
Rabbit anti-NKX2.1	Santa Cruz	sc-13040
Chicken anti-beta Galactosidase antibody	Abcam	Ab9361
Rabbit anti-SM22	Abcam	ab14106
Rabbit anti-Von Willebrand Factor	Abcam	ab6994
Goat anti-VEGFR3/Flt4	R&D	AF743
Rabbit anti-phospho-VEGF Receptor 2 (Tyr1175) (p-VEGFR2)	Cell Signaling	2478
Rabbit anti-VEGF Receptor 2 (VEGFR2)	Cell Signaling	9698
Mouse anti-Claudin 5	Invitrogen	352588
Chemicals, Peptides, and Recombinant Proteins		
Avertin	Sigma	T48402
PFA	Sigma	P6148
OCT	Tissue-Tek	4583
Normal donkey serum	Jackson ImmunoResearch	017-000-121

Continued

REAGENT or RESOURCE	SOURCE	IDENTIFIER
Aquamount	Polysciences	18606
Tamoxifen	Sigma	T5648
Corn oil	Sigma	C8267
Hydrogen peroxide	Sigma	H1009
RPMI	ThermoFisher	11875093
Collagenase Type I (CLS-1)	Worthington	LS004197
Elastase (ESL)	Worthington	LS002294
DNase I (D)	Worthington	LS002007
Fetal bovine serum (FBS)	Invitrogen	10082-139
Trizol reagents	Invitrogen	15596018
0.1% Halt protease and phosphatase inhibitor cocktail	ThermoFisher	78441
Laemmli buffer	BioRad	1610747
4–20% mini-PROTEAN precast gels	BioRad	4561094
Precision Plus Protein Kaleidoscope ladder	BioRad	1610375
Bovine Serum Albumin (BSA)	Sigma	A3059
DMEM media	Corning	10-013-CV
Leibovitz's media	Gibco	21083027
Endothelial cells growth supplement (ECGS)	Cell Applications Inc	212-GS
Penicillin/Streptomycin	Thermo Fisher	15140122
DPBS	Thermo Fisher	14190250
Sheep anti-Rat IgG dynabeads	Thermo Fisher	11035
Recombinant mouse VEGF 120	R&D systems	494-VE-005
Recombinant mouse VEGF 164	R&D systems	493-MV-005
Recombinant mouse VEGF 188	R&D systems	7916-MV-010
Critical Commercial Assays		
RNeasy Micro kit	Qiagen	74004
SuperScript™ IV First-Strand Synthesis System	Invitrogen	18091050
mRNA isolation kit	New England BioLabs	E7490
NEBNext Ultra RNA library prep kit	New England BioLabs	E7530S
SPRIselect reagent kit	Beckman Coulter	B23318
NEBNext® Multiplex Oligos for Illumina	New England BioLabs	E7335S
BCA Protein Assay Kit	ThermoFisher	23225
SuperSignal West Pico Stable Peroxide Solution and Luminol/Enhancer Solution	ThermoFisher	34580
SuperSignal™ West Femto Maximum Sensitivity Substrate	ThermoFisher	34095
Chromium Single Cell 3′ Library & Gel Bead Kit v2	10x Genomics	PN-120267
Deposited Data		
Raw and analyzed data	This paper	GEO: GSE124325
Experimental Models: Organisms/Strains		
Mouse: *Vegfa^LacZ*	Miquerol et al., 1999	NA
Mouse: *Vegfa^CKO* (also called *VEGF-LoxP*)	Gerber et al., 1999	NA
Mouse: *Aqp5^Cre*	Flodby et al., 2010	NA
Mouse: *Hopx^CreER*	Takeda et al., 2011	NA
Mouse: *Sftpc^CreER*	Barkauskas et al., 2013	NA
Mouse: *Cdh5-CreER*	Wang et al., 2010	NA
Mouse: *Shh^Cre*	Harfe et al., 2004	NA
Mouse: *Apln^CreER*	Liu et al., 2015	NA
Mouse: *Rosa^mTmG*	Muzumdar et al., 2007	NA
Mouse: *Rosa^tdT*	Madisen et al., 2010	NA

Continued

REAGENT or RESOURCE	SOURCE	IDENTIFIER
Mouse: $Rosa^{L10GFP}$	Liu et al., 2014	NA
Oligonucleotides		
In situ primers: 5'-TGATCAAGTTCATGGATGTC-3' and 5'-agcttataatacgactcactatagggCTGCATGGTGATGTTGCTCT-3'	This paper	NA
Apln RT-PCR primer: GCCACTGATGTTGCCTCCAG (Forward) GAGCCGGGACCATCAGCAGC (reverse)	This paper	NA
Software and Algorithms		
Imaris 7.7.2	Bitplane	http://www.bitplane.com/imaris
Seurat 2.3.4 (R package)	Butler et al., 2018	https://satijalab.org/seurat.html
Monocle 2.8 (R package)	Qiu et al., 2017; Trapnell et al., 2014	http://cole-trapnell-lab.github.io/monocle-release/docs/
Enhanced Volcano 1.0.1 (R package)	Blighe et al., 2019	https://github.com/kevinblighe/EnhancedVolcano
Prism 7.03	GraphPad Software	www.graphpad.com
FlowJo 10.4.1	FlowJo, LLC	https://www.flowjo.com/
Loupe Cell Browser	10x Genomics	https://support.10xgenomics.com/single-cell-gene-expression/software/visualization/latest/what-is-loupe-cell-browser
Cell Ranger	10x Genomics	https://support.10xgenomics.com/single-cell-gene-expression/software/pipelines/latest/what-is-cell-ranger
ImageJ	Rasband, W.S., ImageJ, U. S. National Institutes of Health	https://imagej.nih.gov/ij/, 1997-2018.
D2 calculator version0.2	Jacob et al., 2009	https://github.com/jamescarson3/computeD2/tree/master/bin
R 3.5.0	The R Foundation	https://www.r-project.org/

LEAD CONTACT AND MATERIALS AVAILABILITY

Further information and requests for resources and reagents should be directed to and will be fulfilled by the Lead Contact, Jichao Chen (jchen16@mdanderson.org). This study did not generate new unique reagents.

EXPERIMENTAL MODEL AND SUBJECT DETAILS

Mice (*Mus musculus*)

The following mouse strains were used: $Vegfa^{LacZ}$ (Miquerol et al., 1999), $Vegfa^{CKO}$ (also called *VEGF-LoxP*) (Gerber et al., 1999), $Aqp5^{Cre}$ (Flodby et al., 2010), $Hopx^{CreER}$ (Takeda et al., 2011), $Sftpc^{CreER}$ (Barkauskas et al., 2013), *Cdh5-CreER* (Wang et al., 2010), Shh^{Cre} (Harfe et al., 2004), $Apln^{CreER}$ (Liu et al., 2015), $Rosa^{mTmG}$ (Muzumdar et al., 2007), $Rosa^{tdT}$ (Madisen et al., 2010), and $Rosa^{L10GFP}$ (Liu et al., 2014). The day of observing a vaginal plug was designated as E1. To induce Cre recombination, tamoxifen (T5648, Sigma) dissolved in corn oil (C8267, Sigma) was injected intraperitoneally. The tamoxifen dosage used is specified in the figure legends. Outliers were excluded only if there were technical errors, such as failed immunostaining. The number of control-mutant pairs and sections analyzed is stated in the figure legends. Unless specified, mice of both genders were used. Investigators were not blind to the genotypes. Control and mutant samples were processed in the same tube or block to minimize experimental variation. No power analysis was used to determine the sample size. All animal experiments were approved by the Institutional Animal Care and Use Committee at Texas A&M Health Science Center Institute of Biosciences and Technology and MD Anderson Cancer Center.

METHOD DETAILS

Antibodies

The following antibodies were used: rabbit anti-Aquaporin 5 (AQP5, 1:2500, ab78486, Abcam), goat anti-Carbonic anhydrase IV (CAR4, 1:500, AF2414, R&D), rat anti-mouse CD31 (1mg/mL, 550274, BD Biosciences), BV786 rat anti-CD31 (1:250, 740870, BD Biosciences),

PE/Cy7 rat anti-CD45 (1:250, 103114, BioLegend), mouse anti-Claudin 5 (Cldn5, 1:500, 352588, Invitrogen), rabbit anti-collagen IV (COL4, 1:2500, LSL-LB-1403, CosmoBioUSA), goat anti-Delta like canonical Notch ligand 4 (DLL4, 1:250, AF1389, R&D), Alexa Fluor 488 rat anti-CD324 (ECAD, 1:500, 53-3249-80, eBioscience), goat anti-Elastin (ELN, 1:500, a gift from Dr. Barry Starcher), goat anti-Endothelial cell specific molecule 1 (ESM1, 1:500, AF1999, R&D), rat anti-endomucin (EMCN, 1:2500, 14-5851-81, eBioscience), rabbit anti-Avian erythroblastosis virus E-26 (v-ets) oncogene related (ERG, 1:5000 for both immunostaining and western blot, ab92513, Abcam), goat anti-Vegfr3/Flt4 (1:1000, AF743, R&D), chicken anti-beta Galactosidase (LacZ, 1:500, Ab9361, Abcam), chicken anti-Green fluorescent protein (GFP, 1:5000, AB13970, Abcam), rabbit anti-Histone H3 (H3, 1:2000 for western blot, 4499, Cell Signaling), Alexa Fluor 647 rat anti-Intercellular adhesion molecule 2 (ICAM2, 1:500, A15452, ThermoFisher), rat anti-Intercellular adhesion molecule 2 (ICAM2, 1:2500, 16-1021-82, eBioscience), goat anti- Intercellular adhesion molecule 2 (ICAM2, 1:500, AF774, R&D systems), eFluor 570 rat anti-Ki67 (1:500, 41-5698-82, eBioscience), rabbit anti-Ki67 (1:1000, RM9106S0, ThermoFisher), rabbit anti-Chondroitin sulfate proteoglycan 4 (CSPG4, 1:1000, AB5320, Millipore), rabbit anti-NK2 Homeobox 1 (NKX2.1, 1:1000, sc-13040, Santa Cruz), rat anti-Platelet derived growth factor receptor alpha (PDGFRA, 1:1000, 14-1401-82, eBioscience), goat anti-Platelet derived growth factor receptor beta (PDGFRB, 1:1000, AF1042, R&D systems), rat anti-Plasmalemma vesicle associated protein (PLVAP, 1:125, 553849, BD Biosciences), rabbit anti-Prospero Homeobox 1 (PROX1, 1:250, 11-002, AngioBio), rat anti-Advanced glycosylation end-product specific receptor (RAGE, 1:1000, MAB1179, R&D systems), rabbit anti-Red fluorescent protein (RFP, 1:1000, 600-401-379, Rockland), Cy3-conjugated mouse anti-alpha-Smooth muscle actin (SMA, 1:1000, C6198, Sigma), rabbit anti-SM22 (TAGLN, 1:2500, ab14106, Abcam), Alexa Fluor 647 rat anti-Vascular endothelial cadherin (VECAD/CDH5, 1:250, 562242, BD Biosciences), rabbit anti-phospho-VEGF Receptor 2 (Tyr1175) (p-VEGFR2, 1:1000 for western blot, 2478, Cell Signaling), rabbit anti-VEGF Receptor 2 (VEGFR2, 1:5000 for western blot, 9698, Cell Signaling), rabbit anti-Vonvon Willebrand Factor (VWF, 1:2500, ab6994, Abcam).

Section Immunostaining
Postnatal lungs were inflation-harvested as described with minor modifications (Yang et al., 2016). Briefly, mice were anaesthetized with Avertin (T48402, Sigma) and perfused through the right ventricle with phosphate-buffered saline (PBS, pH 7.4). The trachea was cannulated and the lung was inflated with 0.5% paraformaldehyde (PFA; P6148, Sigma) in PBS at 25 cm H_2O pressure, submersion fixed in 0.5% PFA at room temperature for 4-6 hr, and washed in PBS at 4 °C overnight. Section immunostaining was performed following published protocols with minor modifications (Alanis et al., 2014; Chang et al., 2013). Fixed lung lobes were cryoprotected in 20% sucrose in PBS containing 10% optimal cutting temperature compound (OCT; 4583, Tissue-Tek) at 4°C overnight and then embedded in OCT. OCT sections at 10 um thickness were blocked in PBS with 0.3% Triton X-100 and 5% normal donkey serum (017-000-121, Jackson ImmunoResearch) and then incubated with primary antibodies diluted in PBS with 0.3% Triton X-100 in a humidified chamber at 4 °C overnight. Sections were washed with PBS in a coplin jar for 1 hr and incubated with donkey secondary antibodies (Jackson ImmunoResearch) and 4′,6-diamidino-2-phenylindole (DAPI) diluted in PBS with 0.3% Triton X-100 at room temperature for 1 hr. After another 1 hr wash with PBS, sections were mounted with Aquamount (18606, Polysciences) and imaged on a confocal microscope (A1plus, Nikon).

Wholemount Immunostaining
This was performed following published protocols with minor modifications (Yang et al., 2016). In brief, ∼3 mm wide strips from the edge of the cranial or left lobes of postnatal lungs or whole lobes of embryonic lungs were blocked with PBS with 0.3% Triton X-100 and 5% normal donkey serum (017-000-121, Jackson ImmunoResearch) and then incubated with primary antibodies diluted in PBS with 0.3% Triton X-100 overnight at 4 °C. The next day, the strips were washed with PBS+1% Triton X-100+1% Tween-20 (PBSTT) on a rocker at room temperature for one hour, and the process was repeated three times. Secondary antibodies and DAPI were added and incubated overnight at 4 °C. On the third day, the strips were washed as described before with PBSTT and fixed with PBS with 2% PFA for at least 2 hr on a rocker. For tissues expressing green or red fluorescent protein, native fluorescence was quenched after immunostaining by overnight incubation with methanol containing 6% hydrogen peroxide (H1009, Sigma) at 4 °C. Finally, the strips were mounted on slides using Aquamount (18606, Polysciences) with the flat side facing the coverslip. Embryonic lungs were also immunostained as a whole and imaged with an optical projection tomography microscope (Bioptonics, UK) as published (Alanis et al., 2014; Chang et al., 2013). Enucleated eyes were fixed in 0.5% PFA for 3-6 hr at room temperature and then retinas were dissected free of retinal pigmented epithelium, lens, and hyaloid vessels, immunostained in the same tube with matching lung strips, and mounted with the vitreous side facing the coverslip. Z-stack images of 20-40 um thick at 1 um step size were taken from the top of the tissue to obtain an en face view.

Section *In Situ* Hybridization
Postnatal lungs were harvested and processed as described for immunostaining except 0.5% PFA was included for the sucrose/OCT overnight incubation to minimize RNA degradation. Colorimetric section in situ hybridization was carried out following published protocols (Alanis et al., 2014; Chang et al., 2013). The entire exon 3 of *Vegfa* was amplified with the following primers for probe: 5'-TGATCAAGTTCATGGATGTC-3' and 5'-agcttataatacgactcactatagggCTGCATGGTGATGTTGCTCT-3' (lower case indicates the T7 promoter sequence). Images were acquired on an upright Olympus BX60 microscope.

Western Blot
Whole lungs were dissected and homogenized in a Dounce homogenizer containing 800 uL of lysis buffer (100 mM NaCl, 20 mM Tris-HCl, 0.5% NP-40, 1 mM EDTA, 0.5% Triton X-100, 1mM PMSF, 1mM NaF, 5mM NaVO3, 0.1% Halt protease and phosphatase

inhibitor cocktail (ThermoFisher, 78441)). Homogenized samples were kept on ice for 10 minutes and then centrifuged at 14,000 rpm for 10 minutes at 4 °C. The supernatant was transferred to a clean tube and protein concentration was determined using a Pierce BCA Protein Assay Kit (ThermoScientific, 23225) following their microplate procedure. 30 ug of protein in 28 uL of Laemmli buffer (BioRad, 1610747) and lysis buffer were separated in a 4–20% mini-PROTEAN precast gel (BioRad, 4561094), along with 10 uL of the Precision Plus Protein Kaleidoscope ladder (BioRad, 1610375), at a constant voltage of 120 V in running buffer (25 mM Tris-HCl, 190 mM glycine, 0.1% SDS, pH 8.3), and were transferred to an Immobilon-PVDF membrane (Merck Millipore, IPVH00010) overnight at a constant current of 0.05 A in transfer buffer (25 mM Tris-HCl, 192 mM glycine, 0.5% SDS, 10% methanol). The next day, the membrane was blocked with 5% Bovine Serum Albumin (BSA, Sigma, A3059) in Tris-buffered saline (TBST; 0.5 M Tris-HCl, 9% NaCl, 0.5% Tween 20, pH 8.4) for 1 hour at room temperature with constant agitation. Primary antibodies were added at the concentration indicated in the antibody section, and incubated overnight at 4 °C. The membrane was then washed three times with TSBT in the course of 1 hr, followed by incubation with a goat anti-rabbit IgG, HRP-linked secondary antibody (1:2000, Cell Signaling, 7074) diluted in 2% BSA in TBST for 1 hr with agitation at room temperature. Finally, the membrane was washed as previously explained. SuperSignal West Pico Stable Peroxide Solution and Luminol/Enhancer Solution (Thermo, 34580) or SuperSignal™ West Femto Maximum Sensitivity Substrate (Thermo, 34095) was added to the membrane for 1 minute, which was then imaged with a BioRad ChemiDoc MP imaging system. When blotting for a second protein, the membrane was washed with TBST before proceeding as described above.

Vasculature Analysis
Wholemount immunostained lung strips as described above were used because this facilitated 3D imaging and segmentation and allowed comparison between equivalent regions. Samples were imaged on a confocal microscope (A1plus, Nikon) using the 40x oil objective with a field size of 318 μm x 318 μm x 20 μm and a pixel dimension of 512 x 512 x 20. At least three confocal Z-stacks per lung were analyzed with Imaris software (Bitplane) to obtain the EC number (ERG) and the percentage of proliferating (KI67) ECs. Surface rendering ICAM2 staining was used to measure vessel volume using the automatic threshold and a cut-off of 50 voxels for both control and mutant lungs. For automatic analysis of CAR4 and PLVAP staining, ERG surface rendering was filtered by the mean intensity of CAR4 or PLVAP, which was then used to mask ERG staining. To measure the EC perimeter, the viewpoint was set for the largest projection area and then all visible cell projections were measured. Cells in contact were split midway between them.

D_2 Air Space Analysis and Mean Linear Intercept (MLI) Analysis
The D_2 index is an area-weighted alveolar diameter that takes into account the heterogeneous distribution of airspace sizes in the mouse lung (Jacob et al., 2009; Parameswaran et al., 2006). In this study, the D_2 was measured and calculated on 5 um-thick frozen lung sections stained with hematoxylin and eosin (H&E). For each mouse, three images were acquired on an upright Olympus BX60 microscope with a 10x objective. Airway and main vessels that could not be avoided during imaging were filled in manually using ImageJ prior to analysis, which was performed using a 225-pixel intensity threshold and a 400-pixel area size cut-off. The same images were used to quantify the mean linear intercept with Photoshop based on a published protocol (Liu et al., 2017). Two horizontal and two vertical gridlines were drawn evenly-spaced on each picture. The distance from one alveolar wall to the next along the gridlines was measured with the Photoshop ruler tool. Airways and main vessels were excluded, as well as alveoli where one wall was not visible in the image. At least 32 intercepts per image and 3 images per mouse were measured.

Cell Dissociation and FACS
Whole lungs were dissected in PBS, minced into pieces with forceps and digested in RPMI (ThermoFisher, 11875093) with 2 mg/mL Collagenase Type I (Worthington, CLS-1, LS004197), 2 mg/mL Elastase (Worthington, ESL, LS002294), and 0.5 mg/mL DNase I (Worthington, D, LS002007) for 30 min at 37 °C. The tissue was mechanically triturated after 15 min of digestion. Fetal bovine serum (FBS, Invitrogen, 10082-139) was added to a final concentration of 20% and the tissue was triturated until homogenous. The sample was transferred to the cold room and kept on ice, filtered with a 70 μm cell strainer (Falcon, 352350), and spun down at 5000 rpm for 1 min. The cells were resuspended in red blood cell lysis buffer (15 mM NH_4Cl, 12 mM $NaHCO_3$, 0.1 mM EDTA, pH 8.0) for 3 min, washed with RPMI with 10% FBS and filtered into a 5 ml glass tube with a cell strainer cap (Falcon, 352235). The cells were then incubated with CD45-PE/Cy7 (BioLegend, 103114), ICAM2-A647 (Invitrogen, A15452), CD31-BV786 (BD Biosciences, 740870) at a concentration of 1:250 for 30 minutes, spun down at 5000 rpm for 1 min, washed for 5 minutes and resuspended with RPMI with 10% FBS. The sample was refiltered and incubated with SYTOX Blue (Invitrogen, S34857), then sorted on a BD FACSAria Fusion Cell Sorter. After exclusion of dead cells and doublets, CD45 negative cells were selected and from those CD31 and ICAM2 positive cells were collected for purified ECs. For scRNA-seq of all 4 lung cell lineages, CD45 positive cells were collected as the immune cell lineage, from the CD45 negative population ICAM2 positive cells were collected as the EC lineage, from the ICAM2 negative population ECAD positive cells were collected as the epithelial cell lineage, and the remaining triple negative population was collected as the mesenchymal lineage. After accounting for a cell-lineage-specific viability factor that was predetermined based on cell survival after FACS, equal proportions of the 4 cell lineages were combined for 10x Genomics library preparation.

RT-PCR and Bulk RNA-Seq
RNA was extracted from FACS-purified ECs using Trizol reagents (Invitrogen, 15596018) and the RNeasy Micro kit (Qiagen, 74004). 100 ng of RNA was used for RT-PCR with the SuperScript™ IV First-Strand Synthesis System (Invitrogen, 18091050). For

CellPress

bulk RNA-seq, 100-200 ng total RNA was used to prepare an RNAseq library using an mRNA isolation kit (New England BioLabs, E7490) and a NEBNext Ultra RNA library prep kit (New England BioLabs, E7530S) with a final double (0.65 x -1 x bead volume) size selection step using a SPRIselect reagent kit (Beckman Coulter, B23318). The libraries were indexed (New England BioLabs, E7335S) and sequenced on an Illumina NextSeq500. Seventy-six nucleotide pair-end reads were generated for each sample and aligned to the UCSC mm10 reference genome using tophat2 and bowtie2 in R (Kim et al., 2013; Langmead and Salzberg, 2012). Transcript abundance, differential expression, and isoform quantitation were calculated using the cufflinks suite in R (Roberts et al., 2011a, 2011b; Trapnell et al., 2013, 2012). Raw data have been deposit in GEO under the accession number GSE124325.

Single-Cell RNA-Seq

FACS-purified lung ECs were processed through the Chromium Single Cell Gene Expression Solution Platform (10x Genomics) using the Chromium Single Cell 3' Library and Gel Bead Kit in accordance with the manufacturer's user guide (v2, rev D). The libraries were sequenced on an Illumina NextSeq500 using a 26X124 sequencing run format with 8 bp index (Read1). Chromium single-cell RNA-seq output was processed with Cell Ranger using "cellranger count" and "cellranger aggr". Further analysis was carried out using Loupe Cell Browser (10x Genomics) or an R package Seurat 2.3.4 (https://satijalab.org/seurat/pbmc3k_tutorial.html). In brief, we selected cells with at least 200 detected genes but no more than 4000 or 5000 genes, depending on the sample's distribution; we also removed cells with more than 5% or 10% mitochondrial genes, depending on the sample's distribution. We then performed log normalization, identification of highly variable genes, scaling, PCA dimensionality reduction, and K-means clustering. Next, we identified differentially expressed genes per cluster and generated tSNE, dot, and violin plots, and heat maps. For volcano plots, the 10x Genomics Cell Ranger Aggregate output file of control and $Vegfa^{CKO/CKO}$; $Shh^{Cre/+}$ mutant samples was processed using Seurat as described before, and then each identified cell type was compared between control and mutant with a pseudocount value of 0.001, a minimal percentage of 0.05, and a log fold change threshold of 0.05. The R package Enhanced Volcano 1.0.1. was used for plotting with a fold change cutoff of 1 and a p value cut off at 10e-5. For trajectory analysis, Car4 and Plvap ECs from individual E17, E19, and P14 scRNA-seq samples were selected using Seurat and then combined and subjected to a canonical correlation analysis (CCA) to account for batch effect. Monocle 2.8 (Qiu et al., 2017) was used to construct a trajectory using the top 439 variable genes obtained in Seurat. Monocle branched expression analysis modeling (BEAM) analysis was used to identify the distinct gene expression patterns. Raw data have been deposited in GEO under the accession number GSE124325.

Primary EC culture

Lungs prior to P7 were processed as described (Wang et al., 2019). In brief, lungs were placed in Leibovitz's media (Gibco, 21083027) and dissociated with collagenase, elastase and DNase as described for FACS. Following incubation in the red blood cell lysis buffer and filtering, the single cell suspension was incubated for 15 minutes at room temperature with Dynabeads (ThermoFisher, 11035) which had been conjugated with a CD31 antibody (0.5 mg/mL, BD Biosciences, 550274). Cells were washed with isolation media (DMEM with 20% FBS and Penicillin/Streptomycin) using a magnetic rack and resuspended in 1.2 mL complete culture media (DMEM, 20% FBS, 1X Endothelial cells growth supplement, 100 μg/ml heparin, Penicillin/Streptomycin). 100 uL of the cell suspension was plated per well in a 0.1% gelatin-coated 12-well plate with a round glass coverslip and cultured at 37 °C in a cell culture incubator with 5% CO_2. Cells were grown for 4 days with media changed every other day until confluent, when the cells were digested with 300 uL of 0.25% Trypsin/EDTA. The reaction was stopped with culture media followed by centrifugation and resuspension in beads washing solution (PBS with 0.1% BSA and Penicillin/Streptomycin). 20 uL of Dynabeads pre-coated with an ICAM2 antibody (0.5 mg/mL, ThermoFisher, 16102182) were added to the suspension and incubated at room temperature for 15 minutes on the rocking platform. Washing and plating was performed as previously described and cells were grown for 1 day and then treated with VEGFA 120, 164 and 188 (100 ng/ml of each; R&D, 494-VE-005, 493-MV-005, 7916-MV-010) added in complete culture media. Media was changed every other day with fresh VEGFA proteins until harvest at day 7 or day 9 post-ICAM2 selection. For staining, media was removed and the cells were fixed onto the glass coverslips with 0.5% PFA. The samples were then blocked with 5% donkey serum in PBST for 1 hour at room temperature. Primary antibodies were added overnight at 4C, followed by a 30 minutes wash in PBS. The samples were incubated with secondary antibodies for 1 hour at room temperature and washed again with PBS. Using forceps, the coverslips were mounted onto slides with Aquamount and imaged on a confocal microscope. ECs were counted based on ERG from at least 2 images per coverslip taken on a stereomicroscope and quantified using ImageJ to obtain the total number of ECs per coverslip. Car4 ECs from the entire coverslip were quantified manually on an upright microscope.

QUANTIFICATION AND STATISTICAL ANALYSIS

Image quantification and statistical testing are described in Method Details for individual experiments. The numbers of biological replicates and significance values are stated in figure legends.

DATA AND CODE AVAILABILITY

Bulk and scRNA-seq data have been deposited in GEO under the accession number GSE124325.